frontiers in Earth Science

ORIGINAL RESEARCH
published: 29 May 2018
doi: 10.3389/feart.2018.00062

An Updated Multi-Temporal Glacier Inventory for the Patagonian Andes With Changes Between the Little Ice Age and 2016

Wolfgang J.-H. Meier, Jussi Grießinger, Philipp Hochreuther and Matthias H. Braun*

Institute of Geography, Friedrich-Alexander-Universität Erlangen-Nürnberg, Erlangen, Germany

We present a satellite-derived glacier inventory for the whole Patagonian Andes south of 45. 5°S and Tierra del Fuego including recent changes. Landsat TM/ETM+ and OLI satellite scenes were used to detect changes in the glacierized area between 1986, 2005 and 2016 for all of the 11,209 inventoried glaciers using a semi-automated procedure. Additionally we used geomorphological evidence, such as moraines and trimlines to determine the glacierized area during the Little Ice Age for almost 90% of the total glacierized area. Within the last ~150 years the glacierized area was reduced from 28,091 ± 890 km^2 to 22,636 ± 905 km^2, marking an absolute area loss of 5,455 ± 1,269 km^2 (19.4 ± 4.5%). For the whole study region, the annual area decrease was moderate until 1986 with 0.10 ± 0.04% a^{-1}. Afterwards the area reduction increased, reaching annual values of 0.33 ± 0.28% a^{-1} and 0.25 ± 0.50% a^{-1} for the periods of 1986–2005 and 2005–2016, respectively. There is a high variability of change rates throughout the Patagonian Andes. Small glaciers, especially in the north of the Northern Patagonian Icefield (NPI) and between the latter and the Southern Patagonian Icefield (SPI) had over all periods the highest rates of shrinkage, exceeding 0.92 ± 1.22% a^{-1} during 2005–2016. In the mountain range of the Cordillera Darwin (CD), and also accounting for small ice fields south of 52°S, highest rates of shrinkage occurred during 1986–2005, reaching values up to 0.45 ± 0.23% a^{-1}, but decreased during the 2005–2016 period. Across the Andean main crest, the eastern parts of the NPI, SPI and adjoined glaciers had in absolute values the highest area reduction exceeding 2,145 ± 486 km^2 since the LIA. Large calving glaciers show a smaller relative decrease rate compared to land-terminating glaciers but account for the most absolute area loss. In general, glacier shrinkage is dependent on latitude, the initial glacier area, the environment of the glacial tongue (calving or non-calving glaciers) and in parts by glacial aspect.

Keywords: Glacier change, Little Ice Age, South America, remote sensing, glacier mapping

OPEN ACCESS

Edited by:
Alun Hubbard,
UiT The Arctic University of Norway, Norway

Reviewed by:
Bethan Joan Davies,
Royal Holloway, University of London, United Kingdom
Jonathan Ryan,
Brown University, United States
Antoine Rabatel,
Université Grenoble Alpes, France

****Correspondence:***
Wolfgang J.-H. Meier
Wolfgang.jh.meier@fau.de

Specialty section:
This article was submitted to Cryospheric Sciences, a section of the journal Frontiers in Earth Science

Received: *31 January 2018*
Accepted: *09 May 2018*
Published: *29 May 2018*

Citation:
Meier WJ-H, Grießinger J, Hochreuther P and Braun MH (2018) An Updated Multi-Temporal Glacier Inventory for the Patagonian Andes With Changes Between the Little Ice Age and 2016. Front. Earth Sci. 6:62. doi: 10.3389/feart.2018.00062

INTRODUCTION

The climate of southwest Patagonia is heavily influenced by the straight zonal band of Westerlies from the Pacific Ocean (Garreaud et al., 2013; Lenaerts et al., 2014). The mountains of the southern Andes form an orographic obstacle perpendicular to the prevalent atmospheric flow. This generates an uplift of humid air masses which results in extreme amounts of precipitation at the windward

side of the orogen (Schneider et al., 2003; Smith and Evans, 2007). Accordingly, precipitation on the western side can exceed up to 10,000 mm a^{-1} (Carrasco et al., 2000; Schneider et al., 2003), whereas the amount rapidly decreases within a distance of ~50–150 km eastwards to <500 mm a^{-1}, thus forming a steep west-east gradient (Carrasco et al., 2002) (**Figure 1**). The vicinity of the Pacific Ocean causes moderate temperatures, yet the vast precipitation rate nourishes many glaciers, constituting the largest temperate ice bodies in the Southern Hemisphere outside the Polar Regions (Aniya, 2013). The main ice bodies of South America, the Northern Patagonian Icefield (NPI) and the Southern Patagonian Icefield (SPI), cover an area of about 4,200 and 13,000 km^2, respectively (Aniya, 1988; Aniya et al., 1992). For both ice fields a continuous retreat has been reported in several studies, except for some unusual advances e.g., by glacier Pío XI (Rivera et al., 1997, 2007; Masiokas et al., 2009b and references therein; Lopez et al., 2010). The 76 major outlet glaciers of the NPI and the SPI typically descent to sea level and are frequently calving into fjords in the west and into lakes to the east, with extraordinary flow velocities up to several km a^{-1} (Sakakibara and Sugiyama, 2014). The tidewater—and lacustrine-calving outlet glaciers are frequently used as indicators of climate change, although they are subject to the influence of more complex glacial—and geomorphologic features leading to an asynchronous behavior (Lopez et al., 2010; Sakakibara and Sugiyama, 2014).

The Federal initiatives of Argentina and Chile document the need for a detailed glacier inventory on a national and/or regional scale that does not only focus on the already well-epresented major ice fields. Glaciers of NPI and SPI solely make up 20% of the total number of 9,429 glaciers (Randolph Glacier Inventory: RGI 6.0) south of 45.5°S (Pfeffer et al., 2014; Randolph Glacier Inventory Consortium, 2017). As the NPI and SPI cover almost 65% of the total glacierized area of southern South America, their contribution to sea level rise is one of the most substantial outside the ice sheets of Greenland and Antarctica (Rignot et al.,

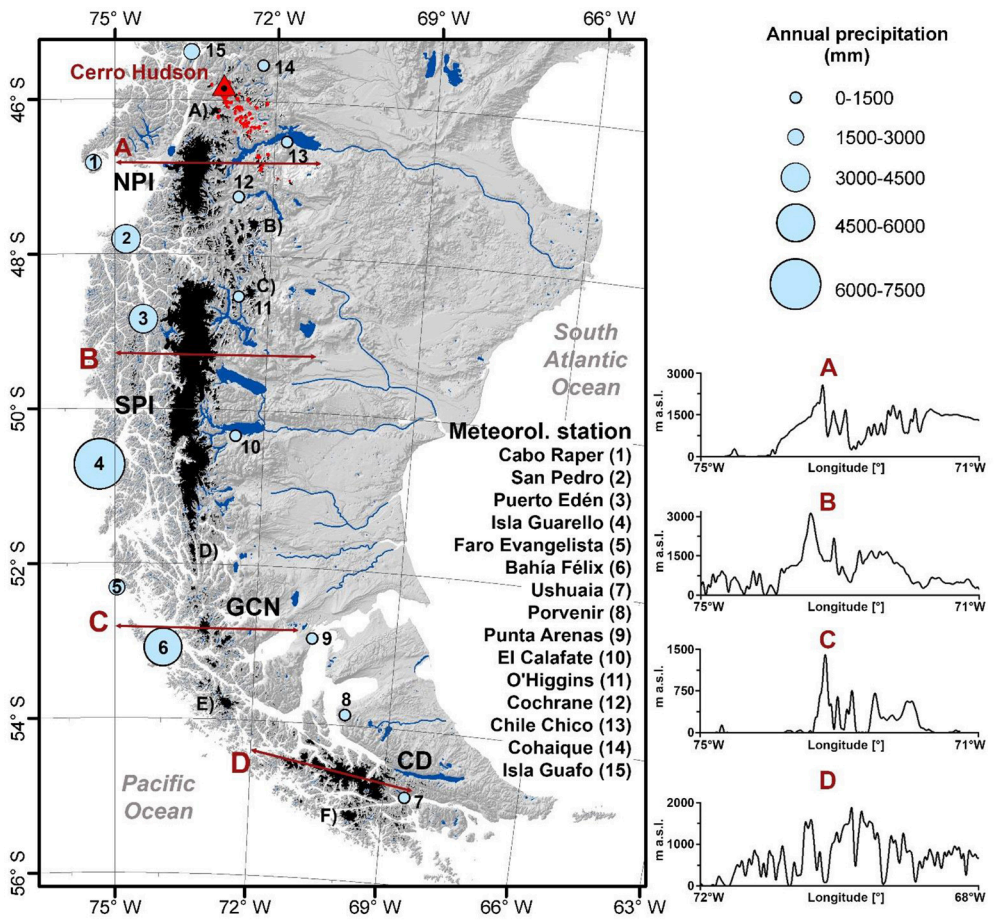

FIGURE 1 | Location of the investigated glacierized area of the Patagonian Andes and Tierra del Fuego with its main ice bodies: Northern Patagonian Icefield (NPI), Southern Patagonian Icefield (SPI), Gran Campo Nevado (GCN), the Cordillera Darwin (CD), and smaller ice bodies: (A) Cerro Erasmo (CE) (B) Monte San Lorenzo (MSL) (C) Sierre de Sangra (SD) (D) Cordillera Sarmiento (CS) (E) Isla Santa Inés (ISI) (F) Isla Hostle (IH). Many glaciers are covered with volcanic deposits due to the eruption of Cerro Hudson in 1991 (red). The high relief energy, displayed by the height transects **(A–D)** transverse to the Andean range and alongside the Cordillera Darwin, leads to high precipitation amounts on the windward side. Eastward of the main ridge, precipitation is rapidly decreasing (Meteorol. data from the Argentinian and Chilean Meteorological Services, lakes from Messager et al., 2016).

2003; Glasser et al., 2011; Malz et al., 2018). Recently, Malz et al. (2018) reported that the SPI solely contributes to the global sea level rise between 2000 and 2015/16 with a mass loss rate equivalent to 0.033 ± 0.006 mm a^{-1}. Geodetic mass balance calculations, as performed by Dussaillant et al. (2018) for the NPI and Malz et al. (2018) for the SPI, require a precise knowledge of the glacial extent. Though the Randolph Glacier Inventory (Pfeffer et al., 2014; Randolph Glacier Inventory Consortium, 2017) is the globally most complete glacier dataset, its accuracy is highly variable and small ice bodies are underrepresented (e.g., Masiokas et al., 2015). Also for larger glaciers (>10 km^2), the glacier outlines and ice divides incorporated in the RGI were not sufficient e.g., for the study of Malz et al. (2018). For this purpose, Dussaillant et al. (2018) had to correct the glacier outlines (taken from the RGI) and ice divides manually, whereas Malz et al. (2018) used an automated mapping approach and also generated new ice divides. Paul and Mölg (2014) named a problematic bias that appears for glacial delineation in the Northern Patagonian Andes from e.g., large amounts of seasonal snow due to the maritime climate and the steep terrain causing widespread cast shadow. Hence, a spatially well-replicated high-resolution dataset of glaciers for the accurate assessment of the regional glacial change in the Southern Andes is still missing.

While studies of individual ice caps (e.g., Rivera and Casassa, 2004; Falaschi et al., 2013) and –fields (Rivera et al., 2007; Schneider et al., 2007; Masiokas et al., 2015) provide a high level of detail, their results are largely incomparable, as they document the state of the local cryosphere at specific points in time, and employ a wealth of methods differing by sensor, approach or thresholds. For example, newly established glacier inventories for the Chilean Andes (Barcaza et al., 2017) performed a glacial change analysis on a small amount of 100 glaciers along a 4,000 km transect for the period 2000–2015 using Landsat TM/ETM+, while Masiokas et al. (2015) report changes of the northeast SPI between 1979 and 2005 using ASTER and ETM+ data for 250 glaciers.

The study of Davies and Glasser (2012) intends to overcome this issue by extrapolating glacier change from the extent during the Little Ice Age (LIA, ∼1870 AD) to the actual extent in 2011, covering the area between 41 and 56°S. Based on a sample depth of 640 manually digitized glaciers, a total area loss of 4,131 km^2 since the LIA was calculated. With 60% of the studied glaciers being outlet glaciers of the major ice fields, the study focuses on the area change of the large glaciers, whereas observed change rates of medium—to small glaciers may be subject to a considerable uncertainty. Additionally, smaller glaciers (<0.1 km^2) were not investigated by Davies and Glasser (2012) and change analysis for 20% of the total glacier number (RGI 6.0) was performed. Consequently, their derived LIA extents are also based on a pixel resolution of 30 m, which justifies the focus on the larger ice bodies. Based on multiple digitization of six glaciers of the NPI an area uncertainty of ± 2% (Davies and Glasser, 2012) was estimated and used for the whole dataset and the whole studied period. This uncertainty value might be questionable, as the relative area error increases strongly with decreasing glacier area (Fischer et al., 2014). In summary, a comprehensive and unbiased glacier inventory, based upon a uniform set of methods, sensor resolution and investigation periods is still lacking for Patagonia. In order to overcome the existing incomparability of local inventories and covering the whole glacierized area of the Southern Andes, we revised and extended the existing glacier inventories for the Patagonian Andes south of 45.5°S including the Tierra del Fuego (**Figure 1**). Based on multi-spectral remote sensing techniques glacier outlines were derived in a semi—automated process from Landsat-5 TM, and Landsat-8 OLI. To assess the regional glacier change, the glacier outlines were inferred for almost all glaciers between the periods 1985/1986, 2005/2006, and 2016/2017. For the LIA, the extents of over 2,500 glaciers were compiled by manual digitization using the Landsat data and additionally Sentinel-2 data from the European Space Agency (ESA). This approach provides a better pixel resolution of 10 m compared to the Landsat data with 30 m. We provide a robust error assessment based on a representative sample of the LIA glacier extents, considering the area class specific area uncertainty. Our LIA glacial extents involve almost 90% of the total glacierized area of 1985/86 thus reveling a change rate assessment during the last 150 years for nearly the whole studied area.

METHODS

Glacier Inventory 1986/87, 2005/2006, and 2016/17

Different techniques for an automated glacier delineation using optical satellite imagery have been successfully applied in various glacierized regions (Andreassen et al., 2008; Bolch et al., 2010a,b). These automated methods provide precise, reproducible and consistent results (Paul et al., 2013) and are well-suited for the examination of larger geographical areas. Since glacier mapping requires as a prerequisite a low surface coverage with seasonal snow and optical sensors are restricted by cloud cover, the availability of suitable satellite scenes from the end of the ablation period is limited. In addition, a small solar altitude angle or inconvenient azimuth angle combined with steep terrain resulting in cast shadows hamper an automated mapping approach. Hence, multiple Landsat satellite scenes for the same periods served as a baseline for our semi-automatic multi-temporal mapping between the periods 1986/87, 2005/2006, and 2016/2017. We used both, Landsat-5 TM and Landsat-8 OLI scenes from the United States Geological Survey (level 1T) for the semi-automated mapping. Due to the failure of the scan line corrector (SLC) the Landsat-7 ETM+ data were not used for the automated approach but serve frequently as well as the Sentinal-2 images as auxiliary data for manual improvement of the outlines, e.g., in shadowed regions (**Figure 2c**) and for seasonal snow.

Since the period of southern hemispheric summer is overlapping parts of two calendar years, we set the respective time span to the starting date of the summer, thus defining the three periods as 1986, 2005, and 2016. In contrast to the recommended GLIMS threshold of 0.01 km^2 as the minimum glacier area (Raup and Khalsa, 2007) we adjusted the minimum threshold in our inventory to ice bodies larger than 0.025 km^2 due to (i)

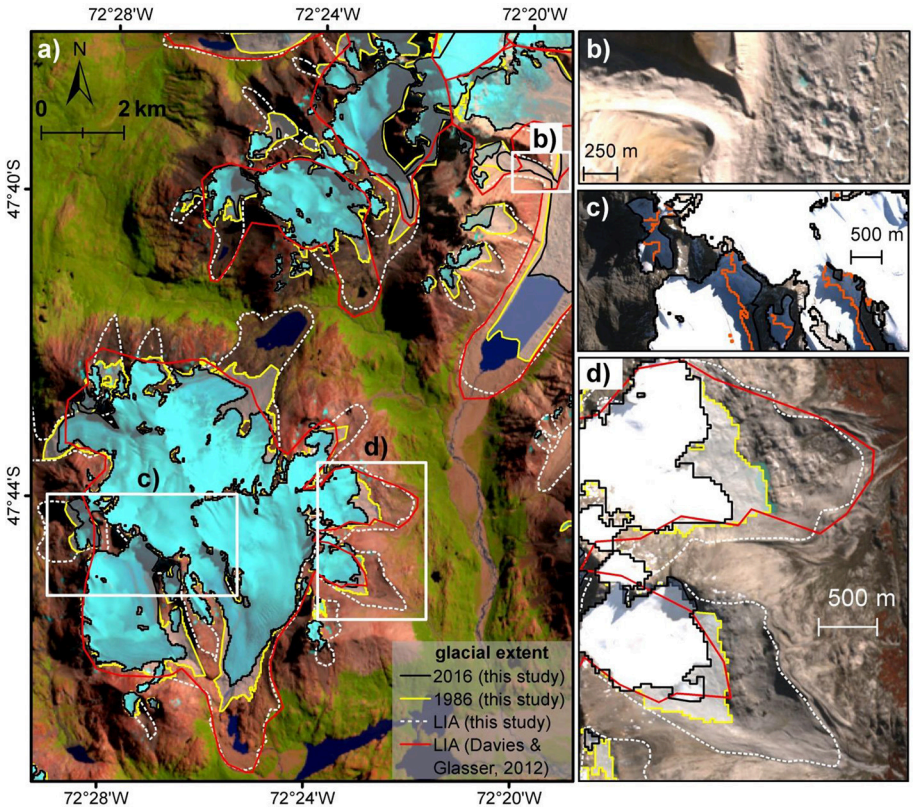

FIGURE 2 | (a) Landsat-8 OLI false color composite (Bands 6,5,4; acquired 05-03-2016) showing the southern part of the Monte San Lorenzo massive (see **Figure 1**) in the north east (Peak of MSL at 47°36'S). Vegetation trimlines are clearly visible for larger valley glaciers. Images (b–d) show magnified sub-regions with Sentinel-2 True Color Image (Bands 2,3,4; acquired 16-04-2017). Black lines represent the manually improved glacier outlines derived from the semi-automated glacier delineation of 2016 (threshold of the TM4/TM6 = 1.8). Ice below a debris cover is visible by ice flow pattern and thermocarst processes **(b)**. The semi-automated mapping reveals good results except for shadowed regions. For the latter **(c)** the original derived outlines (orange) were manually improved. The higher resolution datasets enable the delimitation of several frontal moraine systems **(d)**. In some cases the derived LIA extents from Davies and Glasser (2012) and from this study are very well aligned. But by using better resolved satellite images more LIA glacial extent could be precisely digitized.

the available image resolutions; (ii) a probable misclassification of snow patches; and (iii) a necessary minimum area to detect consistent area changes over the analyzed period.

After re-projecting all scenes to the local UTM zone (18S/19S) for each scene the quality of the orthorectification was checked. Ratio images were calculated by dividing the raw digital numbers for the bands TM3/TM5 (Landsat-5 TM) and TM4/TM6 (Landsat-8 OLI), respectively. The ratio images were converted to a binary image using different threshold values. Starting with a threshold value of 1.0, the value was stepwise increased by 0.1 intervals, ending at a maximum threshold of 3.0. The chosen interval is reasonable since only a few pixel in the outlines change by modifying the threshold by 0.1 (Paul and Hendriks, 2010; Paul et al., 2015). Afterwards, the resulting binary raster was vectorized to generate the glacier polygons without applying any filter. The glacier polygons were compared to a false color composite of the mid-infrared, near infrared and red channels (5-4-3 and 6-5-4, respectively) to obtain the most suitable threshold, mostly ranging between values of 1.7 and 2.2 (**Figure 2a**). The used threshold values and utilized Landsat scene (acquisition date, path/row) are stored within the attributes of the derived respective glacier outline. We created a mask within the already obtained glacier outlines to apply larger thresholds for the band ratio to enhance the assessment of slightly snow-covered rock outcrops. Though water bodies are mistakenly classified as glacier and snow, ratioing the red and mid-infrared channel provided the advantage that glaciers situated in cast shadows could be better delineated than by ratioing of near-infrared and mid-infrared (Paul and Andreassen, 2009). Despite a DEM-derived mask to exclude sea surface in fjords and water bodies >0.1 km^2 from the HydroLAKES database (Messager et al., 2016), a manual correction of the outlines was necessary for nearly every glacier. Additionally, we mapped the shape and area of every lake that was formed between the LIA maximum and 2016 by using the Normalized Difference Water Index (NDWI, threshold value 0.015) and manual mapping.

Suitable scenes since the beginning of the Landsat-5 TM mission, i.e., with only sparse cloud cover and seasonal snow (acquisition date: summer and autumn) were used for a temporal consistency test to distinguish between seasonal snow and small glaciers. Moreover, the use of multi-temporal scenes permitted the manual correction for debris-covered glaciers,

as some glaciological structures, i.e., expanding melting ponds, collapse structures or flow patterns were visible (**Figure 2b**). The glacier outlines were subdivided into individual catchments by extracting the ridgelines and glacier basins using a UTM-projected void-filled DEM with a resolution of 1 arc second (SRTM, LP DACC NASA Version 3). Frequently, the ice bodies reached over the crest of the mountains but are separated by the hydrological basin into distinct individual glaciers. Only if the subsequent ice body exceeds the used threshold value for the glacierized area of 0.025 km^2 we treated them as individual glaciers. At times, drainage basins are ambiguous, hence a few parts of the ice fields are more or less plain in higher elevations and no information about the actual ice flow can be attained by the hydrological basin analysis. Additionally, some large outlet glaciers of the NPI and SPI were subdivided into single glaciers although they share the same hydrological basin. In those cases we used the recently proposed suggestions for glacier divides based on ice flow directions by Mouginot and Rignot (2015).

Due to glacier retreat and the separation and disconnection of former connected glaciers into single basins, our glacier Inventory for 2016 possesses the most subdivides of all periods. For the change analysis, those separated parts were considered as parts of the prior glacier. The Global Land Ice Measurements from Space (GLIMS) identification system based on the latitude/longitude position of a glacier (Raup and Khalsa, 2007) was used and we maintained existing GLIMS IDs were appropriate. The dataset includes all important glacier parameters recommended by Paul et al. (2009). Glacier delineation is aggravated in the northern region of our study area due to the eruption of Cerro Hudson 1991. This event was the second largest Andean volcanic eruption in the twentieth century, causing with an eruptive volume of 8 km^3 heavy ashfall toward the southeast of Patagonia (Scasso et al., 1994; Tilling, 2009). Every single glacier in the studied region was finally inspected visually for errors in misclassification of the band ratio. Additionally, for the year 1986 the automatic glacier delineation in parts of the Gran Campo Nevado and Cordillera Darwin was biased by a high seasonal snow cover and cirrus clouds. The latter still allows a visual identification and distinction of the glacier outlines but is misclassified by an automated mapping. Therefore, in those regions a higher amount of manual mapping and corrections had to be performed.

Determination of the LIA Extent

The Little Ice Age glacial extent was digitized manually, proceeding from the 1986 glacial extent, based on clear visible morphological evidence, e.g., vegetation trimlines or lateral— and terminal moraine systems (**Figures 2a,d**). To avoid an overestimation of the LIA extent, larger rock outcrops (as included in the scenes from 1986) were preserved. Due to its higher resolution compared to Landsat 8 OLI (30 m), data from Sentinel-2 (10 m) were also used for the mapping (**Figures 2b–d**). As proposed by Paul et al. (2013) we also crosschecked our retained glacial extents with high-resolution data from DigitalGlobe. In contrast to other locations like in South Eastern Tibet (Bräuning, 2006; Hochreuther et al., 2015), the ecesis time and thus the vegetation cover on the moraines in the Andes display a higher variation. For example, on the western side of the NPI and SPI, the noted ecesis time varies between 6 and 25 and up to 70 years, respectively (Heusser, 1964; Mercer, 1970; Winchester and Harrison, 1996). In contrast, on the eastern side succession needs between 22 and up to 92 years for the NPI (Winchester and Harrison, 2000; Winchester et al., 2001) and 40 up to 100 years for the SPI, respectively (Pisano, 1978; Dollenz, 1991). In the southernmost regions of Patagonia like Gran Campo Nevado and Cordillera Darwin, the colonization of a recently exposed moraine took <15 and 20 years (Holmlund and Fuenzalida, 1995; Koch and Kilian, 2005). Therefore, we included for the determination of the final LIA glacial extent both completely and partly forest covered terminal moraines.

As the end and also the maximum extent of the LIA is probably variable over the whole study region and local climate conditions as well as different glacial response times can create a bias we define the end of the LIA as 1870 AD for the change calculation. This is consistent with tree ring records for the northern and southern Patagonia, indicating a shift toward warmer temperatures at 1875 (Villalba et al., 2003) and cotemporaneous for the ice retreat and dated moraines (Moy et al., 2009 and references within).

In cases when glaciers formed multiple moraine ridges and trimlines, morphological features were used being closest situated to the recent appropriate glacier (**Figure 2d**). This approach avoids a possible bias caused by an overestimation of the LIA extent. The resulting glacier extent therefore can be considered as a minimum estimation. Finally, our resulting inventory was compared to already published LIA positions (Aniya, 1995, 1996; Holmlund and Fuenzalida, 1995; Kuylenstierna et al., 1996; Harrison and Winchester, 1998, 2000; Winchester and Harrison, 2000; Koch and Kilian, 2005; Araneda et al., 2007; Aravena, 2007; Harrison et al., 2007, 2008, 2012; Strelin and Iturraspe, 2007; Strelin et al., 2008; Masiokas et al., 2009a,b; Glasser et al., 2011; Aniya and Skvarca, 2012; Davies and Glasser, 2012; Rivera et al., 2012).

Uncertainty Assessment

Manual Delineation of the LIA Extent

The LIA glacier outlines were delineated manually and are subject to uncertainties caused by a subjective interpretation and generalization (Paul et al., 2003). Following the guidelines for quality assessment of a glacier area determination (Paul et al., 2017), we estimated the analysts precision by multiple digitization of 360 representative glaciers ranging from 0.04 to 1,100 km^2 with different challenges, e.g., debris cover, floating termini, and cast shadowed regions. The relative digitization inaccuracy commonly increases with decreasing glacier area (Paul et al., 2013; Fischer et al., 2014; Pfeffer et al., 2014). To account for the glacier area distribution of the glaciers in our inventory, we selected the glaciers for the triple digitization in a manner that 85% of them belong to an area-class smaller than 5 km^2. The resulting area-class specific relative mean deviation is much larger for smaller glaciers, resulting in an area uncertainty of $\pm$ 8.4% for glaciers smaller than 0.01 km^2, dropping below $\pm$ 5% when glacier area exceeds 2 km^2 (**Figure 3**). In comparison,

glaciers larger than 5 km^2 only exhibit a mean uncertainty of ± 2.1%.

A second uncertainty factor results from the mapping approach of the LIA maximum extent itself. The moraines and vegetation trimlines that were used for the glacial delineation probably represent the maximum extent of the LIA that does not imperatively reflect the end of the LIA (∼1870 AD). In their review papers Aniya (2013) and Masiokas et al. (2009b) emphasized that the LIA Maximum extent and the end of the LIA occurred contemporaneously for the NPI and nearby glaciers but differ highly for the SPI. For the latter the last LIA maximum was reached until 1800 AD but with a high variability within the 28 studied glaciers to more than 200 years (Masiokas et al., 2009b). For the Magallanes-Tierra del Fuego region the LIA maximum was also reached approximately in 1780 AD but the glaciers stayed still close to the LIA extent until the end of the nineteenth century (Strelin and Iturraspe, 2007; Strelin et al., 2008). A numeric uncertainty estimation of this error is not possible. We tried to keep the error as low as possible by mapping those morphological features closest to the glacier margins (see **Figure 2d**).

Semi-automatic Mapping

Since no appropriate high-resolution reference data is available for the complete dataset and the whole time-span of the investigation period, we determined the precision of our manually improved, semi-automatically derived inventory by applying a positive and negative buffer to the glacier outlines (Granshaw and Fountain, 2006; Bolch et al., 2010a,b). The buffer method accounts for the length of the glacier perimeter, resulting in a higher relative error toward smaller glaciers since those have relatively more edge pixels than larger glaciers (Bolch et al., 2010a; Guo et al., 2015)

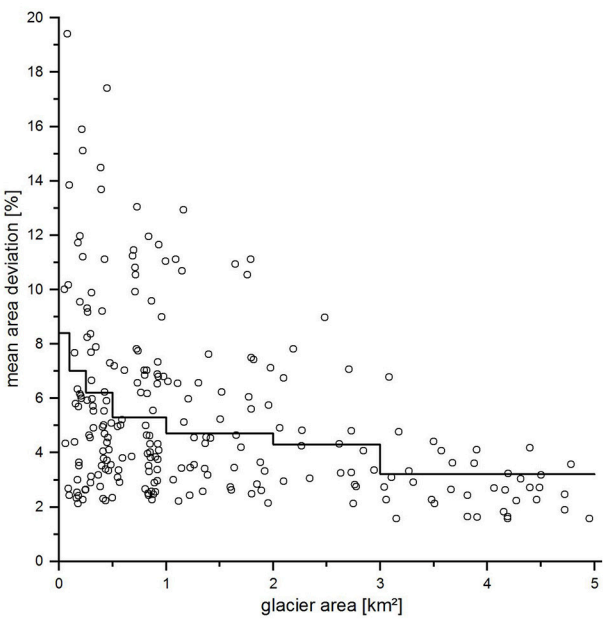

FIGURE 3 | Mean area deviation of 335 multiple digitized glaciers of the LIA extent. Solid line indicates the area class specific uncertainty resulted from fitting a power law by least squares.

The buffer size is dependent on an uncertainly value and is applied to the ice bodies before the intersection with the drainage basins. Consequently, this method will not provide any uncertainty estimations where glaciers adjoin (Paul et al., 2017). Nevertheless, for the ice divides and drainage basins there is probably a small uncertainty, as the former was partly derived from ice flow measurements (Mouginot and Rignot, 2015) and the latter relies on the quality of the DEM, which is susceptible to small errors (Smith and Sandwell, 2003). Omitting these errors at interior ice divides is legitimated since we used the same divides for all investigated time periods. Thus, the total derived area and change rates are not influenced (Pfeffer et al., 2014; Guo et al., 2015; Paul et al., 2017).

The frequently used buffer sizes are ± 0.5 to ± 1 pixel, e.g., ± 15 to ± 30 m (Rivera et al., 2007; Bolch et al., 2010b; Wang et al., 2011). Guo et al. (2015) compared automatically derived and manually improved glacier outlines based on Landsat data to DGPS measurements and revealed an accuracy of ± 18 and ± 11 m, respectively. Following Paul et al. (2013) we compared 15 of our Landsat derived and manually improved glacier outlines to manually delineated glacier outlines from Google Maps™, both from 2016. Every 15 m we calculated the offset between the Landsat and manually derived glacier outlines and obtained a mean offset of 14 m for clean ice bodies. Furthermore, following the same routine as for clean ice bodies, we compared the manually improved glacier outlines for 15 debris covered glaciers, revealing a mean offset of 32 m. Consequently, the use of ± 15 m as buffer size for clean ice and ± 30 m for debris—and ash-covered glaciers is reasonable for our study.

Moreover, the outline accuracy is influenced by the geolocation (i) and the scene quality (ii) of the used satellite data (Paul et al., 2017; Rabatel et al., 2018). To reduce the positional error (i) we align the used Landsat scenes with distinct landforms like moraine ridges, prominent mountain peaks or shorelines revealing an almost perfect matching. Insufficient scene quality (ii) i.e., cloud cover, cast shadow due to low solar angle, and seasonal snow can hamper the automatic measurements and have a huge variability. We minimized those errors by carefully selecting the used Landsat scenes, representing the annual snow minima. Cast shadows and perturbation due to cloud cover were manually edited by the use of different satellite scenes from the same year and the comparison to different sensors like the Sentinel-2 data (**Figure 2c**). In the maritime south western region in rare cases seasonal snow hamper the automated delineation but still allow manual digitization. For those cases, following Bolch et al. (2010a), we applied an additional error of ± 3% to each scene with seasonal snow.

The areal uncertainty for all compiled glaciers of 2016 was ± 4.0%, corresponding to ± 905 km^2, with clean ice bodies having a smaller mean uncertainty than debris covered glaciers with ± 3.6% and ± 5.8%, respectively. Those values are in good agreement with other previous published inventories (Andreassen et al., 2008; Paul and Mölg, 2014). Uncertainty increases toward the smallest and elongated glaciers reaching

values up to ± 70% of the glacier's area. Consequently, the obtained results of the multi-temporal comparison of the Landsat derived glacier outlines must be treated with caution especially for very small glaciers (Paul et al., 2003), fostering our chosen threshold for glacier area larger than 0.025 km^2.

RESULTS

Overview of the Glacier Inventory 2016

In total, our inventory comprises for the year 2016 an amount of 11,209 glaciers (compared to the RGI 6.0: 9,429 individual glaciers) covering a total area of 22,636 ± 905 km^2. The glacierized area is dominated by the major outlet glaciers of the SPI and NPI. In doing so, glaciers larger than 5 km^2 are responsible for 80.7 ± 2.2% of the area, while representing only 3.2% of the total glacier number (**Table 1**, **Figure 4A**). The 30 largest outlet glaciers constitute ∼50% of the total glacierized surface. Here, the largest glacier Pío XI (WGI ID: SPI-137) covers 1,255 ± 5 km^2 (5.5% of the total area). A classification of the inventory by area (**Table 1**) demonstrates, that almost 63% of all obtained glaciers are associated to area classes smaller than 0.25 km^2, representing merely 3 ± 1% of the total glacier area. A further 34% of the glacier number (implies an area of 16.5 ± 2.5%) belongs to the three classes ranging from 0.25 to 5 km^2. The relationship between the number of glaciers per area class and the respective glacierized area is almost perfectly inverted (**Figure 4A**), which additionally supports the significance of the large glaciers for the South American cryosphere. The overall majority of the glaciers and the glacierized area range between 500 and 1,500 m a.s.l., while the average maximum altitude increases with glacier area (**Figures 4B,C**). The average glacier elevation for glaciers north of the Strait of Magallanes is 1,350 m a.s.l.

TABLE 1 | Area classification of the glaciers used in the inventory and the associated summed areas.

Area class [km^2]	Count	Count [%]	Area [km^2]	Area[%]
[0.025; 0.05[	2370	21.1	85 ± 30	0.4
[0.05; 0.1[	2179	19.4	156 ± 31	0.7
[0.1; 0.25[	2472	22.1	402 ± 59	1.7
[0.25; 0.5[	1515	13.5	535 ± 78	2.4
[0.5; 1[	1181	10.5	842 ± 99	3.7
[1; 5[	1134	10.1	2344 ± 189	10.4
[5; 10[	149	1.3	1027 ± 65	4.5
[10; 50[	143	1.3	3038 ± 127	13.4
[50; 100[	29	0.26	1905 ± 58	8.4
[100; 500[	30	0.27	6290 ± 98	27.8
[500; 1000[	6	0.05	4756 ± 71	21.0
≥ 1000	1		1255 ± 5	5.5
Total	11209		22636 ± 905	100

Four hundred fifty-one glaciers are currently calving, of which 93 are of marine (∼20%) and 358 (∼80%) of lacustrine type. We detected 32 dead ice bodies formed due to the disintegration of former glaciers and 17 regenerated glaciers, the latter commonly in steep terrain, with a mean elevation of 545 m a.s.l. far below the average of 1,275 m a.s.l.

Along the longitudinal facing Andean main ridge, over 9,000 glaciers (∼80%) were located within a distance of 1,200 km from north to south (RGI 6.0: 7,447 individual glaciers). The other 20% are situated southeast of the Strait of Magellan within the Cordillera Darwin (CD) and the small icefield of Isla Hostle (IH). On the west side of the Andean crest, the number of glaciers is considerably lower (∼3,200) than in the east (∼5,860). The mean elevation, both for the western and eastern glaciers is decreasing from north to south from a maximum of 1,530 m a.s.l. (Cerro Hudson and Cerro Erasmo) to a minimum with 765 m a.s.l. (Isla Santa Inés). Glaciers toward the west showed a continuous linear descent in their mean elevation ($r^2 = 0.67$) whereas glaciers on the eastern side showed more vertical variability (**Figure 5A**). Conspicuously in the lee of the icefields, the mean elevation displays the highest values whereas, in the fjord-rich area between the NPI and SPI, the mean elevation is decreasing. In the southern part of the SPI (∼51°S) the width of the Andean orogen narrows rapidly from more than 60 to <10 km. At this latitude, a significant decline in the mean elevation for the eastern glaciers is noticeable (**Figure 5A**). In the transitional zone to the Cordillera Sarmiento south of the SPI, the extension of the Andean ridge remains comparatively narrow until 54°S and the mean elevation for western and eastern glaciers only differs slightly.

Two thousand one hundred thirty-five glaciers are located in the Magallanes-Tierra del Fuego (CD, IH) region (RGI 6.0: 1,982 glaciers). The mountain range is predominantly west-east running. As humid air masses originate predominantly from the west and from the south (Holmlund and Fuenzalida, 1995) we divided the study region in a northern part and a southern part of the main mountain ridge. Glaciers north of the main crest have a mean elevation of 900 m a.s.l., 100 m higher than southern glaciers (**Figure 5B**). They also exhibit a weak relationship ($r^2 = 0.37$) of increasing mean elevation with increasing longitude. On the other hand, glaciers that are located south of the range do not show any relationship toward an increasing mean elevation ($r^2 = 0.05$). Nevertheless, the overall elevation for glaciers in the western and eastern parts ($n = 513$ and $n = 300$) reveal an increase from 745 m a.s.l. to 965 m a.s.l. within 250 km.

Glaciers of Southernmost South America

Cerro Hudson and Cerro Erasmo

North of the NPI, larger glaciers are attached to the orographic zones of Cerro Hudson (CH) and Cerro Erasmo (CE). This sub-region is delimited toward the south by a mountain range located north of Rio Exploradores and toward the east by the Lago Buenos Aires. CH is an active volcano characterized by a pronounced caldera with a range of 15 km at 1,900 m a.s.l. The mountain range of Cerro Erasmo is located around 15 km south west of CH with an elevation comparable to CH. A total area of 615 ± 80 km^2 is covered by 1,375 individual glaciers (RGI 6.0: 1,132 glaciers) resulting in a very small mean glacier area of

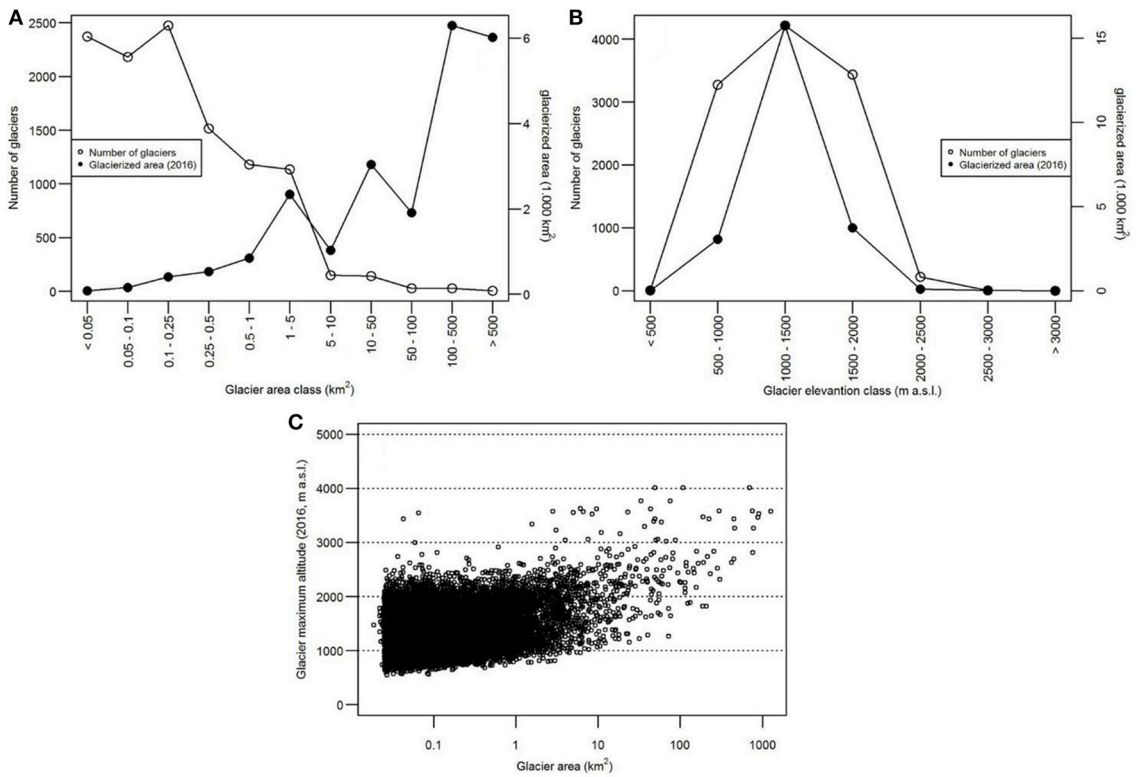

FIGURE 4 | Total glacier number and area with regards to the glacial area class **(A)** and glacier mean elevation class **(B)**. Glacier maximum altitude against glacier area **(C)**.

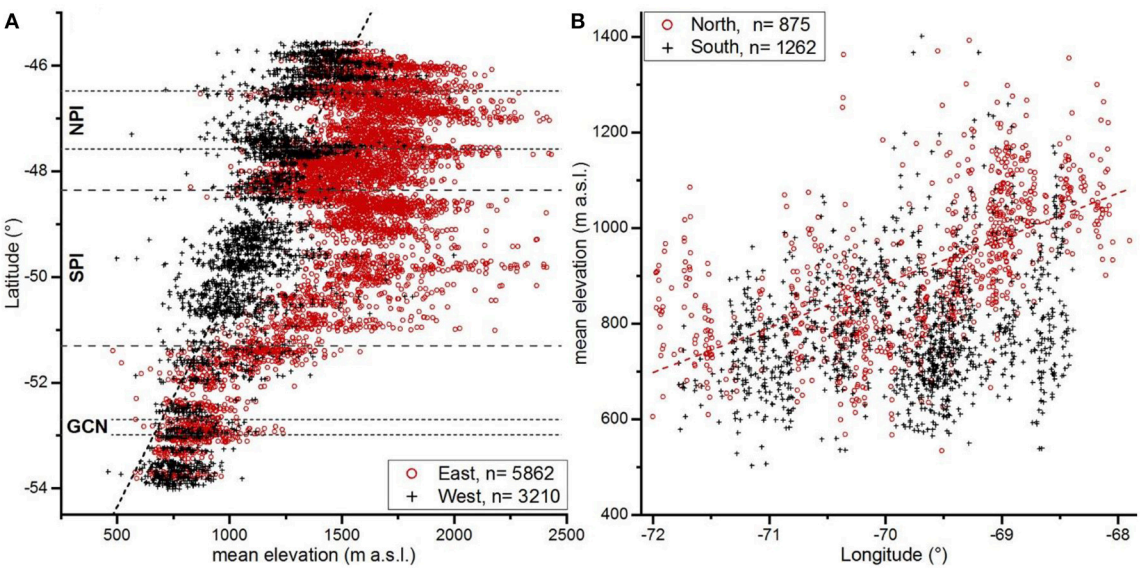

FIGURE 5 | (A) Glacier mean elevation along the north-south running Andean main ridge between 45.5 and 54°S. Glaciers lying west of the main ridge are shown in black, those on the eastern side in red. The dashed/dotted horizontal lines indicate the north-south extent of the main icefields. The regression function explains 67% of the variance distribution for glaciers at the western side of the ice divide. **(B)** Mean elevation of the glaciers along the west east-running mountains of the Cordillera Darwin south of the Magellan Strait (Red and black dots are located north and south of the cordillera, respectively). Dead ice bodies and regenerated glaciers are not included. There is a weak relationship between decreasing longitude and rising glacier mean elevation ($r^2 = 0.37$) for glaciers north of the main ridge.

0.45 km^2. On the one hand the relative high area uncertainty is caused by the overall small glacier area, on the other hand it is the result of volcanic eruption of Cerro Hudson 1991 (Tilling, 2009). Many glaciers toward the southeast are covered with a thick dark layer of tephra (compare **Figure 1**). We could manually identify 150 glaciers which were not or just merely detected by the automated delineation, and mapped them manually and applied afterwards a buffer of ± 30 m. One large outlet glaciers each are descending from the Hudson caldera and from CE toward north western direction. As shown in **Figure 6** (CH, CE) those outlets of CH and CE account for almost 20% of the total glacierized area in this sub-region. Besides those larger glaciers, north-, northwest, and west facing glaciers are lowest in number and area. The majority of all glaciers in terms of total number and area have an aspect between east and south, reaching the local maximum at southeastern exposition (**Figure 6** CH, CE). The glacier mean elevation is 1,570 m a.s.l. reaching the highest values at northeastern and the lowest at southeastern slopes (**Figure 7**). Compared to the NPI and SPI calving glaciers have no major significance in this region, only 30 glaciers were terminating in small lakes.

Northern Patagonian Icefield and Nearby Glaciers

The NPI is the second largest icefield in the Patagonian Andeans covering an area of 3,675 ± 80 km^2. Since the mountain range is north-south striking, most of the glaciers can be assigned to a western or eastern exposition. Glaciers descend from the highest mountain peaks exceeding 4,000 m a.s.l (Monte San Valentin) in the north-eastern part within a short flow length of <50 km to sea level elevation (glacier San Rafael). At the pronounced mountain peak of Cerro Co Arenales (>3,400 m a.s.l) glacier Acodado and glacier Steffen descend toward the southwest. These two glaciers form a large coherent ice body denying an automated

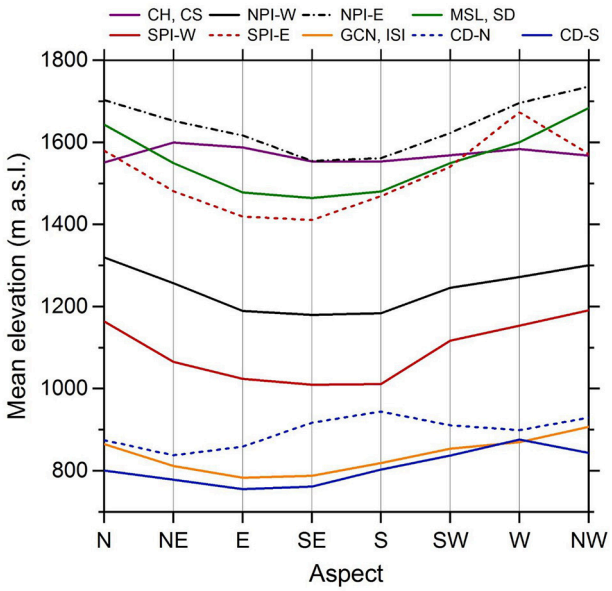

FIGURE 7 | Glacier mean elevation with respect to the glacial aspect for the different sub-regions.

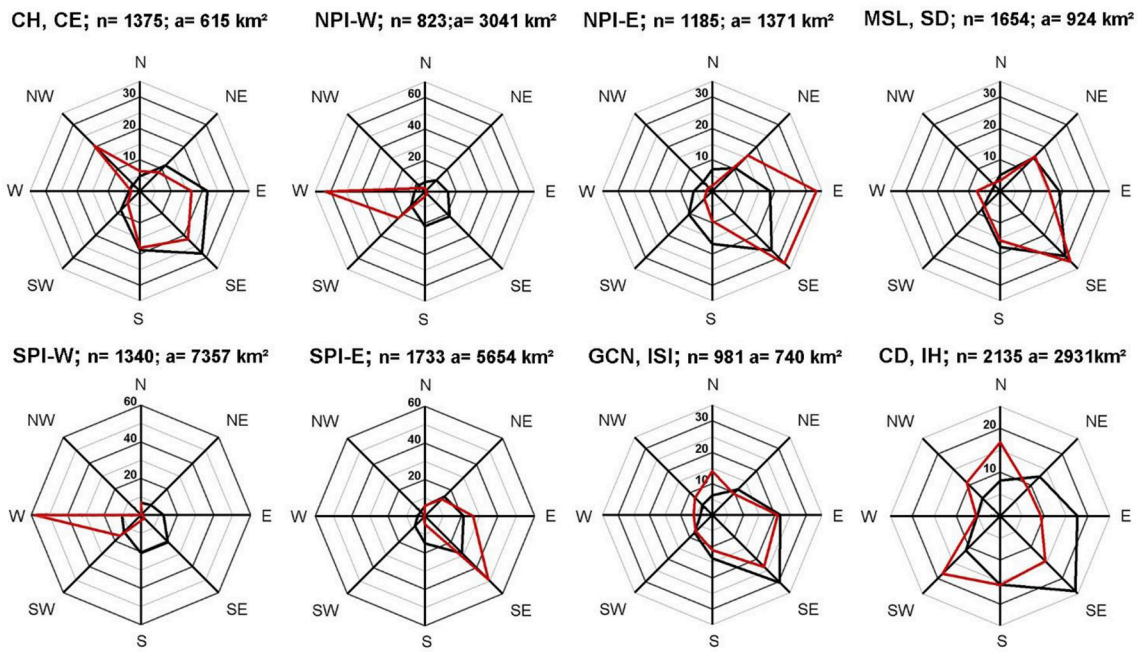

FIGURE 6 | Percentage of glacier number (black) and area (red) for the respective regions in dependence of glacier aspect-class. Number of inventoried glaciers (n) and the total area (a) is given in the respective headline for the different sub-regions. All percentages are based on the particular values of the studied regions (for the used abbreviation refer to **Figure 1**).

watershed delineation and can only be separated by analyzing the ice flow direction (e.g., Rivera et al., 2007; Mouginot and Rignot, 2015). The NPI consists of 171 adjoined (directly connected) glaciers, whereas the 27 major outlet glaciers (>10 km^2) cover 97 ± 1% of the entire icefield. The NPI is surrounded by several 100 of smaller glaciers that are close-by to the icefield but not directly connected. Hence, all adjoined glaciers of the NPI and also nearby located glaciers that are not connected directly to the icefield, were divided in a western and eastern part for further analysis along the Andean crest (**Figure 6**, NPI-W, NPI-E). On the western side, more than 820 glaciers (RGI 6.0: 548 individual glaciers) are nearly equally distributed according their aspect, having a small tendency toward the southeast, but the glacierized area is dominated by the large western outlets (60% of the glacierized area). Across the ice divide, the ∼1,300 glaciers (RGI 6.0: 895 individual glaciers) are prominently facing southeast, but their area is equally distributed with 35% each between the eastern and southeastern aspect. In total 43 glaciers are calving into lakes, the only marine terminating glacier is Glacier San Rafael which is with 758 ± 8 km^2 also the largest of the concerning glaciers. Also 55 debris covered glaciers are predominantly located on the leeward side of the orogen. Glacier mean elevation is lowest for the large outlets toward the western side. On average the mean elevation of glaciers on the windward side is with 1,240 m a.s.l. much lower than the mean elevation for the leeside glaciers with 1,640 m a.s.l. (**Figure 5A**). For both, the western and eastern part, the mean glacier elevation reaches its minimum at east and southeastern exposition with 1,180 and 1,555 m a.s.l, respectively (**Figure 7**).

Southern Patagonian Icefield and Nearby Glaciers

The SPI is the largest of all coherent ice bodies in Patagonia (12,232 ± 201 km^2) with a distance of 350 km north to south, and some summits reaching more than 3,000 m a.s.l. The contiguous ice body of the SPI is composed of 652 individual glaciers that are directly connected. Including also small glaciers that are not directly connected to the SPI but are within the inner perimeter of the icefield as performed by Casassa et al. (2014) reveals a total glacier number of 722 (RGI 6.0: 336 glaciers). Due to the analogous geographical setting of the north-south running Andean mountains, the SPI bears a resemblance of distribution patterns of glacial aspect to area to the NPI and was therefore also divided in a western and eastern part, also including not directly connected mountain glaciers (**Figure 6**, SPI-W; SPI-E). The 150 major outlet glaciers of the SPI and attached valley glaciers have a mainly western or eastern exposition. Around 1,300 glaciers on the western (RGI 6.0: 975 individual glaciers) side are nearly equally distributed according their aspect but the glacierized area is dominated again by the large western outlets (60% of the glacierized area). Across the ice divide, the ∼1,700 glaciers (RGI 6.0: 1,338 individual glaciers) are in number prominently facing southeast and also their area distribution has a similar pattern with 60% of the glacierized area having a southeastern aspect. Those glaciers that have eastern, southeastern and southern aspects indicate the lowest mean elevation (1,440 m a.s.l.) whereas glacier mean elevation increases for western, north-western and northern aspects to 1,625 m a.s.l. A similar distribution for glacier mean elevation is found on the western side of the ice field, though the mean elevation is ∼250 m lower than on the eastern side (**Figure 7**). A small number of debris-covered glaciers could also be identified (n = 65), commonly located on the eastern side.

Monte San Lorenzo and Sierra de Sangra

Between the NPI and SPI the landscape is characterized by large fjord systems and a moderate mean elevation mostly below 1,500 m a.s.l. Toward the Argentinian border, the elevation of the terrain increases, promoting the formation of glaciers. The glacierized area centers around Monte San Lorenzo (MSL) in the north reaching 3,700 m a.s.l. and Sierre de Sangra (SL) in the south with summits up to 2,000 m a.s.l. Both mountain ranges are directly located at the international border between Argentina and Chile. The largest glaciers are found within the two mountain ranges, between them the average glacial area is with 0.5 km^2 comparable small. In total the region between the two major icefields contains 1,654 glaciers (RGI 6.0: 1,393 individual glaciers), covering merely 924 ± 95 km^2 with a preponderantly south-eastern aspect (**Figure 6**, MSL, SD). Glacier mean elevation (**Figure 7**) is lowest (1,450 m a.s.l.) for this aspect class and highest for NW-aspect (1,690 m a.s.l.). Accordingly, the total glacier number is lowest for glaciers with a northwestern aspect (**Figure 6**). 41 of all glaciers are debris-covered, and a further 41 lacustrine-calving.

Minor Icefields (GCN, ISI)

Between the Cordillera Darwin and the southern part of the Cordillera Sarmiento, the average elevation decreases below 2,000 m a.s.l. The whole region is characterized by a high density of fjords and lakes. Toward the south the elevation of the Andean mountain range decreases continuously resulting in mean elevations lower than 1,000 m a.s.l. In contrast to the observed averaged maximum elevation of 1,750 m a.s.l at the SPI, the averaged maximum glacier elevation of 950 m a.s.l is much lower. Despite the comparable low elevation of the Andes there is still a pronounced glacial coverage north and south of the Strait of Magellan. The largest continuous ice body is the Gran Campo Nevado (189 ± 5 km^2) with some outlets calving into the sea, or proglacial lakes. The comparably small ice cap of GCN is surrounded by a large amount of small mountain glaciers. South of the Magellan Strait on Isla Santa Inés (ISI) the second major ice cap (168 ± 5 km^2) of this sub-area is located. In total 981 glaciers were identified for the whole region (RGI 6.0: 1,161 glaciers), which cover a total area of 740 ± 53 km^2. Remarkably, only 25 glaciers account for almost 50% of the total area. 46 glaciers have calving termini (7 marine and 39 lacustrine). Most of the glaciers are classified as clean ice, only 10 glaciers located within the GCN are debris—covered, and five debris-covered glaciers descend from the northern located volcano Monte Burney (S 52.3°, W 73.4°). Within the GCN and ISI, eastern—and southwestern facing glaciers are most frequent (over 50%) and also cover the largest area (**Figure 6**, GCN, ISI). Westerly-exposed glaciers are smallest in terms of number and area. Conversely, they exhibit the highest mean elevation, which drops

from 900 m a.s.l. for west—and northwest exposed glaciers to <780 m a.s.l. for the east—and southeast orientated glaciers (**Figure 7**).

Cordillera Darwin and Isla Hostle

The Cordillera Darwin (CD) is the highest glacierized mountain range in the Tierra del Fuego with several summits reaching more than 2,000 m a.s.l. The CD is frequently seamed by north south running fjords that separate the mountain range in different small parts with steep terrain (see elevation profile in **Figure 1**). The ∼250 km long mountain range is west-east running, hence many of the glaciers have a northern or southern orientation. In total an area of 2,931 ± 155 km^2 is covered by glaciers of which 875 are located at the northern side of main mountain divide and 1,262 south of it (RGI 6.0: 852 and 1,130 individual glaciers, respectively). The largest continuous ice body is located in the center of the mountain range, covering an area of 1,760 ± 51 km^2. Some smaller ice bodies (179 ± 5 km^2), separated by the fjord channels, are located to the west within a short distance to the main ice field. A small icefield (203 ± 6 km^2) is located in the southernmost area of Tierra del Fuego at Isla Hostle (55.1°S). The outlet glaciers of all ice fields frequently descent to sea elevation, and nearly 100 glaciers calve into the numerous fjords. In total, 24 dead ice bodies and regenerated glaciers were identified wherein the largest dead ice body (0.6 km^2) is formed by the disintegration of Glacier Marinelli, the fastest retreating glacier in the CD (Koppes et al., 2009). In total, glaciers facing southeast are most common, but they occupy only a minor area (**Figure 6**. CD, IH). The large outlet glaciers of the longitudinal mountain range typically have a northern or southern aspect; hence they also dominate the area distribution. For glaciers south of the main ridge, the glacial mean elevation is lowest for south and southeastern aspects but reaching a maximum for western expositions.

Glacier Recession Since the Little Ice Age (1870–2016)

The maximum extent of more than 2,600 glaciers during the Little Ice Age was digitized between 45.5 and 55°S. Since many of the former glaciers consist of compound basins and there is no possibility to evaluate the exact date of separation, their initial basins were used for the change detection analysis. The 2,600 LIA maxima contain more than 4,000 of the recent glacier boundaries, which accounts for 35% of the total inventory. This corresponds to 90% of the total glacierized area in 1986. Accordingly, for only 10% of the glacierized area in 1986, no LIA maximum could be detected. In order to provide a minimum estimation of the total LIA extent for all glaciers, we added the glacial extents derived in 1986 for the missing 10% of the glacierized area. From 1986 to 2016, we provide change rates for all glaciers south of 45.5°. Only for few glaciers at the most western locations a multi-temporal comparison was not possible since suitable satellite images were not available. Consequently, the respective 186 glaciers (45 km^2) were excluded from the change analysis.

Nearly 2,200 out of the 2,600 digitized LIA extents are located in the Patagonian Andes, of which 200 completely vanished by 1986 (**Figure 8A**). Out of the sum of 420 recorded LIA maxima within the Cordillera Darwin, only 18 glaciers disappeared. Those were all land-terminating small glaciers in the eastern part of the Cordillera. The 182 glaciers that disappeared north of the Strait of Magellan are all located on the eastern side of the Andean main crest. The total number of glaciers that completely vanished since the LIA increases toward the north, with the majority (141) located north of 48°S. The most frequent glacier aspect for those glaciers is southeast, east and south. Only 41 glaciers had different expositions. **Figure 8A** shows the relative area change for the 2,600 LIA glaciers between 1870 and 2016. Nearly all glaciers (90%) that disappeared had an area smaller 0.5 km^2 and in general larger glaciers exhibit a smaller relative area decrease than smaller ones.

Overall Change Rates

Since the Little Ice Age, the glacier area decreased from 28,091 ± 890 km^2 to 22,636 ± 905 km^2 in 2016. These results display an absolute area loss of 5,455 ± 1,269 km^2 (19.4 ± 4.5%). Following the suggestions by Bolch et al. (2010a) we summarized area changes for the periods 1870–2016, 1870–1986, 1986–2005, and 2005–2016, and 1986–2016 (**Table 2**). The strongest annual area decrease appeared between 1986 and 2005 with an average area loss of 0.33 ± 0.28% a^{-1}. Between 2005 and 2016 glacier recession was comparable high at 0.25 ± 0.50% a^{-1}. Due to the high uncertainty values these two change rates do not differ significantly. Between 1986 and 2016 the glaciers loss in average an area of 0.29 ± 0.17% a^{-1}, whereas between 1870 and 1986 the decrease rate of 0.10 ± 0.04% a^{-1} is slightly smaller.

On average, calving glaciers show the lowest percentage of area reduction in the period between the LIA and 2016. For the 2,600 known LIA extents, land-terminating glaciers had an area reduction of 0.41 ± 0.10% a^{-1}, whereas marine and lacustrine calving glaciers at the same time merely decreased by 0.15 ± 0.08% a^{-1}. However, the calving glaciers are commonly the largest in the study region, consequently the total average area reduction for calving glaciers is with 0.07 ± 0.02 km^2 a^{-1} ten times higher than for the smaller terrestrial ending glaciers. A total of 1,159 newly formed lakes and the enlargement of prior existing LIA lakes was mapped resulting in an increase of the total lake surface area of 889 km^2. There is a strong relationship between glacial shrinkage and the resulting lake area ($r^2 = 0.78$). Over 650 LIA glaciers of area class smaller than 0.5 km^2 had a relative area reduction of more than 75% within the last 150 years. Larger glaciers up to 5 km^2 still suffer of an enormous decrease of more than 50% (**Figure 8A**). With increasing glacier area the relative surface degradation decreases, simultaneously the absolute values for area loss reaches their maximum. A surface loss of more than 1,000 km^2 for only 9 glaciers equals nearly one fifth of the total area degradation of the studied region.

Within the last 30 years, the total glacierized area decreased by 8.8 ± 5.1% from 24,818 ± 912 km^2 to 22,636 ± 905 km^2 (**Table 2**) and a total number of 192 glaciers completely disappeared. **Figure 8B** indicates a higher percentage area loss for smaller glaciers. Most glaciers that have melted down entirely are smaller than 0.1 km^2 and even glaciers up to 0.8 km^2 completely disappeared. On the other hand, plenty of glaciers of area class

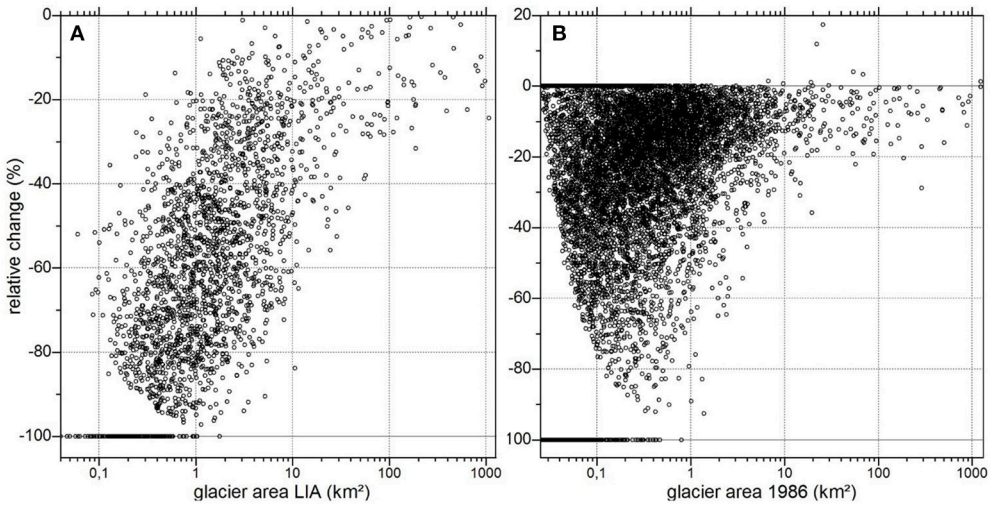

FIGURE 8 | relative area change for the moraine-derived LIA glaciers ($n = 2616$) between 1870 and 2016 depended on the initial glacier area **(A)** and relative area change between 1986 and 2016 in dependence of the initial glacier area in 1986 **(B)**.

TABLE 2 | Decrease in glacier area for the inventoried glaciers between LIA and 2016 for different time periods to derive annual change rates for the studied region.

Year	Area [km^2]	Period	Area change [km^2]	Area change [%]	Annual change [km^2 a^{-1}]	Annual change [% a^{-1}]
1870	28090.8 ± 890.1	1870–2016	−5454.7 ± 1269.3	−19.4 ± 4.5	−37.36 ± 8.69	−0.13 ± 0.03
1986	24817.9 ± 912.3	1870–1986	−3272.4 ± 1274.6	−11.6 ± 5.1	−28.21 ± 10.99	−0.10 ± 0.04
2005	23277.1 ± 907.2	1986–2005	−1540.8 ± 1286.6	−6.2 ± 5.2	−81.10 ± 67.72	−0.33 ± 0.28
2016	22635.6 ± 904.9	2005–2016	−641.5 ± 1281.3	−2.8 ± 5.5	−58.32 ± 116.48	−0.25 ± 0.50
		1986–2016	−2182.3 ± 1284.9	−8.8 ± 5.2	−72.74 ± 42.83	−0.29 ± 0.17

0.25–1 km^2 did not show a noticeable decline over the same period.

Only 13 glaciers showed an advance during the last decades, the rest is either constant or retreating (**Figure 8B**). The majority of the advancing glaciers (10 out of 13) are located in the Cordillera Darwin and all belong to the marine-calving type. Glacier Pío XI and a small tributary south of it account for significant advances at the west side of the SPI. The latter glacier is the only terrestrial terminating glacier that shows a recent advance. Glacier Pío XI is the only known glacier that exceeds its glacier's Neoglacial maximum extent and is under scientific focus since 1830 (Warren et al., 1997 and literature within). Finally, on the eastern side of the SPI, the Perito Moreno glacier shows an advance but solely of small dimension. Across the whole study area, it is apparent that smaller glaciers indicate a greater percentage of loss between 1986 and 2016. Glaciers ranging from 0.1 to 1 km^2 ($n = 5{,}168$) lost on average 20% of their initially glacierized area. Conversely, glaciers larger than 50 km^2 ($n = 66$) decreased by 1,197 ± 164 km^2 in total, corresponding to 8.2% of their original area. Glacier shrinkage is not only restricted to the lower ablation zones but also occurs in high elevation zones due to dry calving of steep hanging glaciers and ice aprons. Also, the expansion of internal rock outcrops over the observation period is frequently seen in the accumulation areas of larger glaciers, indicating a glacial thinning. Small glaciers show the highest variability in relative surface reduction ranging between equilibrium and total decay.

Table 3 and **Figure 9** give an overview of glacier shrinkage since the LIA for the respective studied regions. Glacial recession was highest in the area north of the NPI for the Cerro Hudson und Cerro Erasmo region. The relative area reduction was highest for the sub-regions of CH, CE and MSL, SD, revealing an area reduction of 48 ± 11% and 42 ± 10% since the LIA. For the period between 1870 and 1986 those inventoried regions showed the highest relative change rates of the whole inventory, according to 0.27 ± 0.10% a^{-1} and 0.24 ± 0.09% a^{-1}. In both cases the annual change rate increases from from 3.26 ± 1.24 km^2 a^{-1} and 3.96 ± 1.49 km^2 a^{-1} for 1870–1986 to 6.35 ± 3.38 km^2 a^{-1} and 6.91 ± 4.25 for 1985–2016. Due to the high uncertainty value those accelerated shrink rates are statistically not significant and a more or less constant area reduction since the LIA is also probable. In total the CH, CE and MSL, SD sub-regions lost 1,236 ± 298 km^2 since the end of the LIA (**Table 3**). Especially glacier area classes ranging from 0.1 to 1 km^2 exhibit the largest area loss (30%) within the last 30 years. Glaciers with an eastern—and southeastern exposition suffered the greatest

TABLE 3 | Area changes for the respective studied regions for different time periods (1870, 1986, 2005, 2016).

Year		Area change [km^2]	Area change [%]	Annual change [$km^2 a^{-1}$]	Annual rate [% a^{-1}]		Area change [km^2]	Area change [%]	Annual change [$km^2 a^{-1}$]	Annual rate [% a^{-1}]
LIA-16	CH, CE	−568.5 ± 133.5	−48.0 ± 11.3	−3.89 ± 0.91	−0.33 ± 0.08	NPI -W	−570.7 ± 118.9	−15.8 ± 3.3	−3.91 ± 0.81	−0.11 ± 0.02
LIA-86		−377.9 ± 143.2	−31.9 ± 12.1	−3.26 ± 1.24	−0.27 ± 0.10		−301.5 ± 123.0	−8.3 ± 3.4	−2.60 ± 1.06	−0.07 ± 0.03
86–05		−121.1 ± 105.8	−15.0 ± 15.4	−6.37 ± 5.57	−0.79 ± 0.69		−174.4 ± 103.2	−5.3 ± 3.1	−9.18 ± 5.43	−0.28 ± 0.16
05–16		−69.5 ± 92.1	−10.1 ± 15.0	−6.32 ± 8.38	−0.92 ± 1.22		−94.9 ± 98.3	−3.0 ± 8.6	−8.63 ± 8.94	−0.28 ± 0.28
86–16		−190.6 ± 101.5	−23.6 ± 12.6	−6.35 ± 3.38	−0.79 ± 0.42		−269.2 ± 107.9	−8.1 ± 3.3	−8.97 ± 3.60	−0.27 ± 0.11
LIA-16	NPI -E	−715.1 ± 173.3	−34.3 ± 8.3	−4.90 ± 1.19	−0.23 ± 0.06	MSL, SD	−667.1 ± 165.2	−41.9 ± 10.4	−4.57 ± 1.13	−0.29 ± 0.07
LIA-86		−545.4 ± 181.5	−26.1 ± 8.7	−4.70 ± 1.56	−0.22 ± 0.08		−459.9 ± 173.2	−28.9 ± 10.9	−3.96 ± 1.49	−0.24 ± 0.09
86–05		−92.4 ± 147.0	−6.0 ± 9.5	−4.87 ± 7.74	−0.32 ± 0.50		−148.9 ± 130.9	−13.2 ± 11.6	−7.83 ± 6.89	−0.69 ± 0.61
05–16		−77.3 ± 136.8	−5.3 ± 9.4	−7.02 ± 12.43	−0.48 ± 0.85		−58.3 ± 120.1	−5.9 ± 12.2	−5.31 ± 10.92	−0.54 ± 1.11
85–16		−169.7 ± 142.5	−11 ± 9.2	−5.66 ± 4.75	−0.37 ± 0.31		−207.2 ± 127.5	−18.3 ± 11.3	−6.91 ± 4.25	−0.61 ± 0.38
LIA-16	SPI -W	−791.0 ± 171.2	−9.7 ± 2.1	−5.42 ± 1.17	−0.07 ± 0.02	SPI -E	−1430.0 ± 313.7	−20.2 ± 4.4	−9.79 ± 2.15	−0.14 ± 0.03
LIA-86		−323.3 ± 177.8	−4.0 ± 2.2	−2.79 ± 1.53	−0.03 ± 0.02		−924.5 ± 320.6	−13 ± 4.5	−7.97 ± 2.76	−0.11 ± 0.04
86–05		−334.7 ± 177.2	−4.3 ± 2.3	−17.62 ± 9.32	−0.23 ± 0.12		−382.6 ± 274.8	−6.2 ± 4.5	−20.14 ± 14.46	−0.33 ± 0.24
05–16		−133.0 ± 170.6	−1.8 ± 2.3	−12.09 ± 15.51	−0.16 ± 0.08		−123.0 ± 266.7	−2.1 ± 4.6	−11.17 ± 24.24	−0.19 ± 0.42
85–16		−467.7 ± 176.2	−6.0 ± 2.3	−15.59 ± 5.87	−0.2 ± 0.08		−505.5 ± 279.8	−8.2 ± 4.5	−16.85 ± 9.33	−0.27 ± 0.15
LIA-16	GCN, ISI	−143.3 ± 58.3	−16.2 ± 6.6	−0.98 ± 0.40	−0.11 ± 0.05	CD-N	−315.8 ± 64.2	−18.8 ± 3.8	−2.16 ± 0.44	−0.13 ± 0.03
LIA-86		−59.9 ± 62.3	−6.8 ± 7.1	−0.52 ± 0.54	−0.06 ± 0.06		−159.8 ± 70.0	−9.5 ± 4.2	−1.38 ± 0.61	−0.08 ± 0.04
86–05		−49.1 ± 54.4	−6.0 ± 6.6	−2.59 ± 2.86	−0.31 ± 0.35		−130.7 ± 64.8	−8.6 ± 4.1	−6.88 ± 3.44	−0.45 ± 0.23
05–16		−34.3 ± 49.8	−4.4 ± 6.4	−3.12 ± 4.52	−0.40 ± 0.58		−25.3 ± 57.6	−1.8 ± 4.1	−2.30 ± 5.23	−0.16 ± 0.37
85–16		−83.5 ± 53.9	−10.1 ± 6.5	−2.78 ± 1.80	−0.34 ± 0.37		−156.0 ± 64.0	−10.2 ± 4.2	−5.20 ± 2.13	−0.34 ± 0.14
LIA-16	CD-S	−254.4 ± 60.3	−14.0 ± 3.3	−1.74 ± 0.41	−0.10 ± 0.02					
LIA-86		−123.5 ± 86.9	−6.8 ± 4.8	−1.06 ± 0.75	−0.06 ± 0.04					
86–05		−106.7 ± 80.1	−6.3 ± 4.7	−5.61 ± 4.22	−0.33 ± 0.25					
05–16		−24.3 ± 50.2	−1.5 ± 3.2	−2.21 ± 4.56	−0.14 ± 0.29					
85–16		−131.9 ± 66.3	−7.7 ± 3.9	−4.36 ± 2.21	−0.26 ± 0.13					

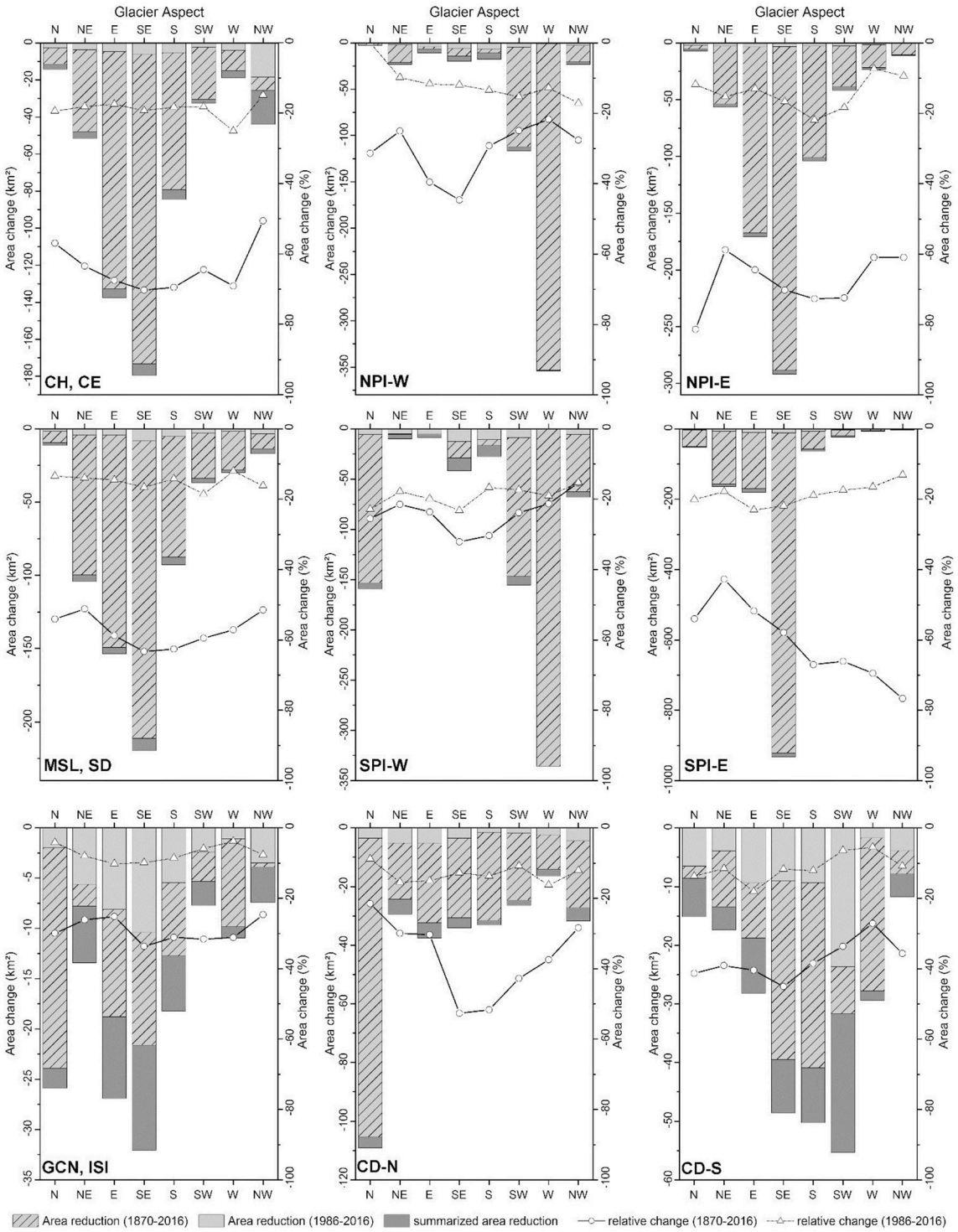

FIGURE 9 | Absolute (bars) and relative (lines) area loss since the LIA, dependent on glacial aspect. Anytime no LIA extent could be digitized, the glacial area of the 1986 derived inventory was used.

loss in terms of total area and relative area (**Figure 9**: CH, CE; MSL, SD). The LIA extents for the majority of all glaciers of those sub-regions were manually digitized, only a few ones had to be interpolated by using the outlines from 1986. But at the volcano Cerro Hudson the LIA outline of the major outlet glacier could not be determined hence the induced lahars due to the eruption in 1991 devastated the moraine systems (**Figure 9**, CH, CE, NW-aspect).

Since the LIA, the western NPI and SPI lost the bulk of their area through western-exposed glaciers, whereas these were the ones with low relative change rates (**Figure 9**: NPI-W, SPI-W). In total, the western parts of the NPI and SPI and adjoined glaciers reveal an area reduction of 1,361 ± 290 km^2 since the LIA, whereas the glacierized area in the eastern parts was reduced by 2,145 ± 487 km^2 (**Table 3**). Until 1986 the area loss since 1870 was moderate for the NPI-W and SPI-W with 2.60 ± 1.06 $km^2\ a^{-1}$ and 2.79 ± 1.53 $km^2\ a^{-1}$, respectively. In both cases the annual area change increased between 1986 and 2016, reaching a maximum of 15.59 ± 5.87 $km^2\ a^{-1}$ at the SPI. The eastern part of the NPI and adjoined mountain glaciers reveal an area loss of 715 ± 173 km^2 since the LIA. Including all uncertainties the annual change rates are more or less constant ranging between 4.70 ± 1.56 $km^2\ a^{-1}$ and 7.02 ± 12.43 $km^2\ a^{-1}$. Annual change rates of the eastern part of the Andean main crest at the SPI are nearly twice as high as for the NPI-E according to 7.97 ± 1.6 $km^2\ a^{-1}$ between 1870 and 1986 and 16.85 ± 9.33 $km^2\ a^{-1}$ for the period of 1986–2016.The total area loss for the eastern part of the SPI accounts for 1,430 km^2 since the LIA and is the largest of the whole investigated region. For both regions the total area loss was highest for southeast and eastern facing glaciers (**Figure 9**, NPI-E and SPI-E). For the entire inventory, the glaciers of the GCN, ISI sub-region shows the lowest total area reduction since the LIA (143 ± 59 km^2). Simultaneously, the area loss rate between the LIA and 1986 was the lowest (0.06 ± 0.06% a^{-1}) of all measured sub-regions (**Table 3**). Yet as shown in **Figure 9** digitizing the LIA extents was frequently not possible due to the glaciers calving into fjords and the lack of moraines. Therefore, many glacial extents of 1986 fill this gap, leading to possible bias. Nevertheless, during the last 30 years the glacial area is also subject to high loss rates reaching values up to 0.40 ± 0.58% a^{-1}. For the northern CD, glaciers with northern aspect are responsible for the highest amount of area loss, while south-/southeast-exposed glaciers have the highest relative loss rates (**Figure 9**, CD-N). On the southern declivity, southeast to southwest expositions dominate the area change, whereas the relative are change reaches its maximum for southeast facing glaciers. The northern as well as the southern part of the CD reveal a low area reduction of 0.08 ± 0.04 and 0.06 ± 0.04% a^{-1} between the LIA and 1986, respectively. Glacier shrinkage accelerates slightly since 1986 to 0.34 ± 0.14 and 0.26 ± 0.13% a^{-1}, respectively.

It is additionally apparent that for smaller glaciers (<10 km^2) the reported relative change is higher than for larger glaciers. In absolute values, however, the large glaciers make a huge contribution to the reduction in surface area. For example, the area loss of 791 ± 171 km^2 for the SPI-W between LIA and 2016 is dominated by only 15 of the 1,300 glaciers that account for over 65% of the area change.

DISCUSSION

Our semi-automated acquisition of all South American glaciers south of 45.5° offers the possibility to compare and verify numerous previous studies that focused on single or multiple glacial settings, or aimed at inferring complete inventories. In total our glacier inventory contains 11,209 individual glaciers in 2016, whereas the RGI 6.0 provides a total of 9,429 glaciers for the same region (Pfeffer et al., 2014; Randolph Glacier Inventory Consortium, 2017). On the one hand we inventoried 867 additional glaciers (∼75 km^2), on the other hand, 2,729 RGI glaciers (corresponding to 308 km^2) are not incorporated in our new inventory. This large difference cannot be explained by the different glacier area thresholds that were used in the both inventories. Only 640 of the 2,729 glaciers (RGI 6.0) are smaller than 0.025 km^2 and are therefore not included in our inventory. The remaining 2,089 glaciers are either misclassified seasonal snowfields which have been rejected by our temporal consistency test, in rare cases wrongly classified water bodies, or glaciers which already disappeared since the turn of the millennium. The glaciers that are included in both inventories also differ in total number due to the small-scaled drainage basin analysis that was performed in our updated inventory. The RGI 6.0 inventoried a total of 6,700 glaciers, whereas we subdivided those glaciers into 10,344 individual entities. The resulting differences in the individual glacier catchment areas and different investigation periods aggravate a direct comparison of the particular glaciers. For our studied region the total area estimation provided by the RGI 6.0 is with 25,452 km^2 even larger than our estimated glacierized area of 24,818 ± 912 km^2 in 1986 (23,277 ± 907 and 22,636 ± 905 km^2 in 2005 and 2016, respectively). Even considering the glacierized area of 308 km^2 that we did not record in our inventory and an additionally mapped area of 168 km^2 of rock outcrops (refers to 1986) than comprised in the RGI 6.0 the difference in the two datasets still can exceed 1,000 km^2 (refers to the glacierized area of 2005). Those differences can only be attributed to our manually improvement of the automatic derived outlines, whereas many glaciers in the RGI were not adequately enhanced. A glacier inventory in 2001 was performed by Rivera et al. (2007) and De Angelis (2014) for the NPI and SPI, respectively. For the NPI 70 glaciers larger than 0.5 km^2 were detected, covering an area of 3,953 km^2 in 2001 (Rivera et al., 2007, **Table 4**). In our study the NPI is assembled of 171 individual glaciers (>0.025 km^2) covering an area of 3,806 ± 80 km^2 in 2005. The number of large outlet glaciers is not modified between the two datsets rather the glacierized area at the outer perimeter of the icefield was subdivided particularly. De Angelis (2014) considered for the SPI 139 glaciers larger than 5 km^2 covering an area of 12,363 km^2 in 2001. In our inventory (2016) the SPI is assembled of 128 glaciers larger than 5 km^2 and over 500 smaller glaciers that were excluded by De Angelis (2014) covering an area of 12,232 ± 201 km^2 (**Table 4**).

Most studies which provide not only an inventoried dataset but also include a change assessment of the glacierized area focus predominantly on the NPI and SPI. **Table 4** lists the results from our study for the NPI, SPI, and two smaller catchments in comparison to previous published results. The small catchments are located at the eastern side of the Andean main crest at MSL and Lakes San Martín (LSM). Dussaillant et al. (2018) calculated the glacierized area of the NPI for 2000 and 2012 with 3,856 ± 211 km^2 and 3,740 ± 200 km^2, respectively. Their calculated area loss of 116 ± 290 km^2 (3 ± 7.5%) is in good agreement with our

TABLE 4 | Comparison of the inventoried glacierized areas and change rates for the NPI, SPI and sub-regions of the MSL (Monte San Lorenzo) and LSM (Lakes San Martín).

	Year	Area [km^2]	Period	Area loss [km^2]	Area loss [%] [%]	Area loss [km^2 a^{-1}]	Area loss [% a^{-1}]	Source
NPI	1870	4457.6 ± 79.2	1870–16	−782.8 ± 112.2	−17.6 ± 2.5	−5.36 ± 0.77	−0.12 ± 0.01	This study
NPI	1986	4004.5 ± 77.6	1870–86	−453.2 ± 110.8	−10.2 ± 2.8	−3.90 ± 0.96	−0.09 ± 0.02	This study
NPI	2005	3806.3 ± 79.7	1986–05	−198.2 ± 111.2	−5.0 ± 2.8	−10.43 ± 5.85	−0.26 ± 0.15	This study
NPI	2016	3674.9 ± 79.5	2005–16	−131.4 ± 112.0	−3.5 ± 3.0	−11.95 ± 10.23	−0.31 ± 0.27	This study
NPI	1870	4635 ± 93	1870–11	−659.7 ± 112.1	−14.2 ± 2.6	−4.68 ± 0.87	−0.10 ± 0.02	Davies and Glasser, 2012
NPI	1986	4142 ± 83	1870–86	−493.4 ± 124.3	−10.6 ± 3.0	−4.25 ± 1.07	−0.09 ± 0.03	Davies and Glasser, 2012
NPI	2001	4070 ± 81	1986–01	−72.1 ± 116.1	−1.7 ± 2.9	−5.15 ± 7.74	−0.12 ± 0.19	Davies and Glasser, 2012
NPI	2011	3976 ± 80	2001–11	−94.1 ± 113.8	−2.3 ± 2.9	−8.55 ± 11.38	−0.23 ± 0.29	Davies and Glasser, 2012
NPI	2000	3856 ± 211	2000–12	−116 ± 290	−3.0 ± 7.5	−9.66 ± 24.16	−0.25 ± 0.63	Dussaillant et al., 2018
NPI	2012	3740 ± 200						Dussaillant et al., 2018
NPI	1979	4093	1979–01	−140 ± 61	−3.4 ± 1.5	−6.36 ± 2.77	−0.15 ± 0.07	Rivera et al., 2007
NPI	2001	3953						Rivera et al., 2007
SPI	1870	14208.0 ± 184.3	1870–16	−1976 ± 272.8	−13.9 ± 1.9	−13.54 ± 1.86	−0.10 ± 0.01	This study
SPI	1986	13043.9 ± 186.9	1870–86	−1164.0 ± 262.5	−8.2 ± 2.0	−10.03 ± 2.27	−0.07 ± 0.02	This study
SPI	2005	12485.6 ± 199.4	1986–05	−558.4 ± 273.3	−4.3 ± 2.1	−29.38 ± 14.38	−0.23 ± 0.11	This study
SPI	2016	12231.7 ± 201.1	2005–16	−253.9 ± 283.3	−2.0 ± 2.3	−23.08 ± 25.75	−0.18 ± 0.21	This study
SPI	1870	14862 ± 122	1870–11	−1644 ± 122	−11.1 ± 0.8	−11.65 ± 0.87	−0.08 ± 0.01	Davies and Glasser, 2012
SPI	1986	13657 ± 124	1870–86	−1205 ± 124	−8.1 ± 0.9	−10.38 ± 1.07	−0.07 ± 0.01	Davies and Glasser, 2012
SPI	2001	13424 ± 116	1986–01	−233 ± 116	−1.7 ± 0.9	−15.53 ± 7.74	−0.11 ± 0.06	Davies and Glasser, 2012
SPI	2011	13218 ± 113	2001–11	−206 ± 206	−1.5 ± 0.9	−18.73 ± 11.38	−0.15 ± 0.09	Davies and Glasser, 2012
SPI	1986	13003 ± 282	1986–00	−489 ± 377	−3.8 ± 2.9	−34.93 ± 26.93	−0.27 ± 0.21	Casassa et al., 2014
SPI	2000	12514 ± 250						Casassa et al., 2014
LSM	1870	246.6 ± 9.1	1870–16	−73.8 ± 12.7	−29.9 ± 5.2	−0.50 ± 0.08	−0.20 ± 0.03	This study
LSM	1986	194.1 ± 8.3	1870–86	−52.5 ± 12.0	−21.3 ± 6.2	−0.45 ± 0.10	−0.18 ± 0.05	This study
LSM	2005	178.0 ± 8.2	1986–05	−16.0 ± 11.3	−8.3 ± 6.3	−0.84 ± 0.59	−0.43 ± 0.33	This study
LSM	2016	172.8 ± 8.1	2005–16	−5.2 ± 12.0	−2.9 ± 7.0	−0.48 ± 1.09	−0.27 ± 0.63	This study
LSM	1870	423.2 ± 8.5	1870–16	−102.9 ± 10.6	−24.3 ± 2.5	−0.73 ± 0.08	−0.17 ± 0.02	Davies and Glasser, 2012
LSM	1986	365.9 ± 7.3	1870–86	−57.2 ± 11.2	−13.5 ± 3.0	−0.49 ± 0.10	−0.12 ± 0.03	Davies and Glasser, 2012
LSM	2001	364.3 ± 7.3	1986–01	−1.6 ± 10.3	−0.4 ± 2.8	−0.11 ± 0.69	−0.03 ± 0.19	Davies and Glasser, 2012
LSM	2011	320.2 ± 6.4	2005–16	−44.1 ± 9.7	−12 ± 3.0	−4.0 ± 0.97	−1.21 ± 0.30	Davies and Glasser, 2012
LSM	1979	220.9 ± 7.4	1979–05	−33.7 ± 9.9	−15.3 ± 4.5	−1.29 ± 0.38	−0.59 ± 0.17	Masiokas et al., 2015
LSM	2005	187.2 ± 7.4						Masiokas et al., 2015
MSL	1870	322.5 ± 10.1	1870–16	−137.0 ± 12.7	−42.5 ± 3.9	−0.93 ± 0.09	−0.29 ± 0.03	This study
MSL	1986	225.3 ± 9.2	1870–86	−97.1 ± 12.0	−30.1 ± 5.3	−0.84 ± 0.10	−0.26 ± 0.04	This study
MSL	2005	199.2 ± 9.1	1986–05	−26.1 ± 11.3	−11.5 ± 5.0	−1.37 ± 0.60	−0.60 ± 0.27	This study
MSL	2016	185.4 ± 10.1	2005–16	−13.8 ± 12.0	−6.9 ± 6.0	−1.26 ± 1.09	−0.63 ± 0.55	This study
MSL	1870	265.3 ± 8.4	1870–11	−83.2 ± 10.6	−31.3 ± 4.0	−0.59 ± 0.08	−0.22 ± 0.03	Davies and Glasser, 2012
MSL	1986	192.5 ± 7.3	1870–86	−73.8 ± 11.2	−27.4 ± 5.8	−0.62 ± 0.1	−0.24 ± 0.05	Davies and Glasser, 2012
MSL	2001	184.7 ± 7.3	1986–01	−7.8 ± 9.7	−4.1 ± 5.6	−0.56 ± 0.69	−0.27 ± 0.30	Davies and Glasser, 2012
MSL	2011	182.1 ± 6.4	2001–11	−2.6 ± 9.7	−1.4 ± 5.3	−0.24 ± 0.97	−0.14 ± 0.53	Davies and Glasser, 2012
MSL	1985	239	1985–08	−44 ± 13	−18.6 ± 5.9	−1.9 ± 0.6	−0.81 ± 0.26	Falaschi et al., 2013
MSL	2000	215	1985–00	−24 ± 13	−9.9 ± 5.3	−1.6 ± 0.8	−0.66 ± 0.35	Falaschi et al., 2013
MSL	2008	195	2000–08	−21 ± 13	−8.7 ± 5.3	−2.6 ± 1.6	−1.09 ± 0.66	Falaschi et al., 2013

derived glacier outlines between 2005 (3,806 ± 80 km^2) and 2016 (3,675 ± 80 km^2), indicating an area loss of 3.5 ± 3.0%. Between 1979 and 2001 Rivera et al. (2007) estimated an area decrease of 3.4 ± 1.5% for the NPI whereas we estimate an area decrease by 5.0 ± 2.9% between 1986 and 2005. The least area reduction was calculated for the periods of 1986–2001 and 2001–2011 by Davies and Glasser (2012) according to 1.7 ± 2.9% and 2.3 ± 2.9%, respectively. As stated, a direct comparison of our study with the previous studies is problematic, since the area of the NPI was measured at different times, the applied methods are diverse, and the uncertainty values differ highly. For 2000/2001 three area estimations of the NPI (**Table 4**) were performed, revealing a mean deviation of ± 107 km^2. This comparable high mean deviation is an important issue concerning the reliability of the calculated area change and change rates that vary in the same magnitude (**Table 4**). Our nearest area estimation of the NPI in terms of time (2005) is with 3,806 ± 80 km^2 around 150 km^2 smaller than the estimated areas of 2000/2001. But also for the same investigation time of 1986 our estimated area is ∼140 km^2 smaller than the derived outlines by Davies and Glasser (2012). We attribute those regional differences that apply to the whole inventory to four factors: first the definition of the respective ice fields or study regions differ. Davies and Glasser (2012) as well as Schneider et al. (2007) for the GCN, include glaciers at the perimeter of the ice fields that were, according to our LIA maxima moraine mapping, not connected to the ice field itself even during this cooler period. In addition, Casassa et al. (2014) also include single glaciers within the inner perimeter of the SPI to the icefield even when they are not directly connected to itself. Our inventory assigns only those glaciers to the respective ice field which were directly connected with it at least during the LIA. Secondly, the newly available, multi-season remote sensing data that were used in our study enable the recognition of small catchments and moraine settings, as well as the differentiation of temporal snow fields, firn basins and small glaciers. We assume, that existing studies might thus have overestimated the truly glacierized area. Thirdly, other regional inventories, e.g., Masiokas et al. (2015) and Barcaza et al. (2017) include in their inventory ice bodies larger 0.01 km^2 whereas our study provides only ice bodies larger 0.025 km^2. Finally, the amount of rock outcrops included in the previous inventories and that were excluded from the glacierized area in our study contributes a substantial spatial difference, as already described by Rivera et al. (2007) for the inventory of Aniya (1988). The rock outcrops could be one of the major error sources between the different inventories. For 2001 rock outcrops for the NPI were estimated as 120 and 175 km^2, respectively (Rivera et al., 2007; Davies and Glasser, 2012). Our inventory contains for the interior rocks in 1986 and 2005 an area of 205 km^2 and 231 km^2, respectively.

For the SPI our results are in good accordance to the area estimation of Casassa et al. (2014) with nearly the same area in 1986 (**Table 4**). Also, the calculated change rates, although not for the same periods are nearly the same, whereas Davies and Glasser (2012) calculated only one half of our estimated area loss within the last 30 years (**Table 4**). Our obtained glacierized area in 1986 and 2005 of the sub-region LSM and MSL, respectively, lie within the uncertainty value provided by the previous inventories (**Table 4**, LSM, MSL). Taking every uncertainty into account, the discrepancies in the glacierized area estimation between the outlines derived by Davies and Glasser (2012) and our study are very high, exceeding a relative difference of 50% for the LSM sub-region (**Table 4**, LSM). In 2005 our estimated area of the LSM sub-region (178 ± 8 km^2) is in good agreement with the previously calculated area of 187 ± 7 km^2 for the same investigation period (Masiokas et al., 2015), whereas Davies and Glasser (2012) measured an area of 364 ± 7 km^2 in 2001 (**Table 4**). Our estimated area loss of 26 ± 11 km^2 between 1986 and 2005 for the MSL sub-region is equivalent to the area reduction of 24 ± 13 km^2 between 1986 and 2001 (Falaschi et al., 2013) and is twice as high as measured by Davies and Glasser (2012) for 1986–2001 (**Table 4**).

Table 4 corroborates also the differences in the LIA extents between the inventories that exceed several hundred km^2. For the same studied region, Davies and Glasser (2012) obtain by the sample-based calculation of the LIA extent a total area of 25,939 ± 518 km^2. In contrast, our detected extent of 28,091 ± 890 km^2 is by 8.3% significantly larger. The LIA extents from the prior study were adapted to our drainage basins to ensure a comparability of the two data sets. The glacial extents represented in both studies differ largely with an area difference exceeding 4000 km^2 for the same glacierized regions. On the one hand we digitized a larger area of 1,280 km^2, on the other hand Davies and Glasser (2012) included 2,750 km^2 that are not contained in our inventory. Those area differences arise from various factors: first, some LIA glacial extents are subject of controversial scientific debate, e.g., LIA extents in the fjords of Bahia Pía, Cordillera (Kuylenstierna et al., 1996; Koch, 2015). As we want to provide a reliable minimum estimation of the LIA extent we used the estimated area provided by Kuylenstierna et al. (1996) for the glaciers in the Bahia Pía which are significant smaller than the outlines by Davies and Glasser (2012). Secondly, we preserved larger rock outcrops (as included in the inventory from 1986) to avoid an overestimation of the glacierized area, leading to an area exceeding 1,300 km^2, whereas Davies and Glasser (2012) estimated 310 km^2 of interior rock outcrops. At last, in some cases we could not find sufficient morphological evidence for the prior derived outlines and did not include them. Alternately existing outlines could be improved by higher resolution data (see **Figure 2d**). For the glaciers larger than 100 km^2 the relative difference between the two studies is with ± 3.8% comparably small but those values rapidly increase with decreasing glacier area leading to a mean relative difference of ± 30% for glaciers ranging between 5 and 10 km^2 and even exceeding up to more than 100% for small glaciers. Our study provides 1760 LIA glacial extents that were not included in previous inventories, covering an area of 2,249 ± 110 km^2. Those newly derived outlines could probably not be mapped by Davies and Glasser (2012) due to the lack of high resolution data, since these glaciers are fairly small: 61% of those new generated LIA extents belong to the glacier area class smaller than 1 km^2 covering an area of 506 ± 30 km^2. For 3,976 glaciers inventoried in the RGI 6.0 study region (corresponds to 42% of the glaciers) we could therefore identify the LIA glacial extent, whereas the study by Davies and Glasser (2012)

determined the LIA extent for 1881 (20%) of the RGI 6.0 glaciers.

The sub-regions of CH, CE, and MSL, SD show the highest relative area loss since the LIA according to a relative area reduction of 48 ± 11 and 42 ± 10%, respectively. At the same time those sub-regions possess the smallest glacial mean area. This is in good agreement with other findings, indicating larger relative area decrease for small glaciers within the last decades (Masiokas et al., 2015). At the same time Masiokas et al. (2015) emphasize the high variability of shrinkage rates (0–100%) for smaller glacier units. We observed this high variation also in our complete studied region, especially for glaciers smaller than 1 km^2 (**Figure 8B**). Frequently those glaciers that reveal a small relative shrinkage are situated in couloirs, at exposed slopes combined with dry calving or in shadowed cirques, favoring their preservation (Falaschi et al., 2013). For the MSL sub-region Falaschi et al. (2013) report an increase in area loss between 1985 and 2000 and 2000 and 2008 according to 1.6 and 2.6 $km^2\ a^{-1}$, respectively. In this study, no absolute area uncertainties are provided, but the authors used the same error estimation as in our inventory, consequently the margin of uncertainty are nearly the same (**Table 4**). In absolute values we confirm those results but given the large error term and the short time period of change assessment the values are not statistically significant. Davies and Glasser (2012) state the increasing shrinkage for the NPI and SPI twice as high in the recent years than between 1870 and 1986 reaching a maximum between 2001 and 2011. It could be problematic to assume a real acceleration within the recent decades since the uncertainty values of ± 2% by Davies and Glasser (2012) or the area loss calculation by Casassa et al. (2014) for the SPI with 489 ± 377 km^2 between 1986 and 2000 reveal that the area reduction rates are within the uncertainty range (**Table 4**). On the other hand, we can support the acceleration in the recent area loss rates compared to the period between the LIA and 1986. However, the derived annual shrinkage rates have to be regarded with caution, as the assumption of a constant shrinkage rate between the LIA maximum and 1986 is fairly unlikely. It is also possible that within the period between LIA and 1986 there were many sub-periods where glacier shrinkage was faster or even much slower. Additionally many calving glaciers are variable due to non-climatic factors and do not show a constant behavior, e.g., several of the glaciers of the Cordillera Darwin reveal an advance since 1986 whereas the surrounding land-terminating glaciers al retreated. Considering all uncertainty values it could be also possible for the whole studied region as one, that the glacier recession is more or less constant since the end of the LIA. On the other hand some morphological features that were used for the LIA mapping could be far older than 1870 as expressed in the uncertainty assessment. Then it is possible that the shrinkage rates are even smaller than our calculated values.

For the other major ice fields like CD, IH, and ISI Bown et al. (2015) derived from ASTER and Landsat ETM+ data between 2001 and 2011 an area of 2,331, 274, and 273 km^2, respectively. In total 1,681 glaciers were identified covering an area of 3,289 km^2. Our study estimates for the same region with 3,169 km^2 in 2005 identifying over 2,400 individual glaciers. Although the differences of both independent derived inventories seem to be small (∼120 km^2), they are very important concerning the change analysis. For example within the last 30 years we measured an area reduction of 287 ± 130 km^2 for the Cordillera Darwin and adjoined glaciers, including IH and ISI, which is only twice as high as the uncertainties between two derived inventories.

With respect to local factors, our data supports the findings of Davies and Glasser (2012) that calving glaciers show the smallest rates of shrinking, and smaller glaciers shrink faster on average. Considering aspect, for the whole inventory, southeast-oriented glaciers showed the highest annual retreat, whereas we could not find a significant west-east gradient in this manner. The latter is in accordance with findings of Davies and Glasser (2012), just as the absolute rate of area loss being highest with glaciers with western aspect. This is especially remarkable, since this not only includes the mainly west-east-oriented, large glaciers of the NPI and SPI, but the whole inventory.

The total area change reflects mainly the differences in the two largest glacier area classes (>100 km^2; 42 glaciers account for 40.2% of the total area change, and in the glaciers between 1 and 5 km^2 in area (20.4%). The former is in accordance with Rivera et al. (2007), who report for the the NPI that e.g., Glaciar San Quintín alone accounted with 33 km^2 for a large part of the total area change of 140 km^2 between 1979 and 2001.

CONCLUSION/ SUMMARY

A large scaled glacier inventory was derived for the whole Patagonian Andes south of 45.5°S and Tierra del Fuego. In 2016 a total 11,209 glaciers, covering an area of 22,636 ± 905 km^2 were inventoried. Compared to other inventories that contain our whole study region, we identified due to our detailed basin analysis a surplus of nearly 2000 glaciers (compared to the RGI 6.0). The SPI and the NPI are the largest temperate ice bodies in South America, covering an area of 12,232 ± 201 and 3,674 ± 80 km^2, respectively. Most of the glaciers have a south-eastern aspect, but larger outlet glaciers depend on the large scale orientation of the mountain ranges. The outlet glaciers are frequently perpendicular orientated to the longside mountain range, resulting in western and eastern aspect for the NPI and SPI and a north and south aspect for the CD. Change analysis for the whole glacierized area was done for 1986, 2005, and 2016 indicating an area loss of 8.6% (2,182 ± 1,276 km^2) within the last 30 years. Additionally, the glacial extent for over 2600 glaciers during the Little Ice Age was derived resulting in a glacial cover of 28,091 ± 890 km^2. Overall glacier shrinkage increased for the periods 1870–1986, 1986–2005, 2005–2016 from 0.10 ± 0.04 to 0.33 ± 0.28% a^{-1} ending at 0.25 ± 0.50% a^{-1}, respectively. The relative area loss was highest for smaller glaciers. In total over 600 glaciers completely disappeared since the Little Ice Age and over 650 glaciers reveal an area reduction of over 70%. Beside the glacier area, glacial retreat is influenced by latitude and terminating environment. Glacier shrinkage was highest in the northern parts of our study region. Also, between the two largest icefields and east of them, relative decrease in area was highest for small glaciers. Glaciers of the Cordillera Darwin were

retreating fastest between 1986 and 2005; afterwards the rate of glacial shrinkage decreased. Land-terminating glaciers showed the highest and most continuous retreat, whereas calving glaciers are more variable due to non-climatic factors, e.g., calving process and bedrock topography.

AUTHOR CONTRIBUTIONS

WM performed the glacial delineation and performed subsequent analysis together with PH and JG. MB initiated and supervised the study and wrote jointly with WM the manuscript.

FUNDING

This study was funded by the joint CONYCET-BMBF research project GABY-VASA: Responses of Glaciers, Biosphere and Hydrology to Climate variability and climate change across the Southern Andes (grant no. 01DN 15020).

REFERENCES

Andreassen, L. M., Paul, F., Kääb, A., and Hausberg, J. E. (2008). Landsat-derived glacier inventory for Jotunheimen, Norway, and deduced glacier changes since the 1930s. *Cryosphere* 2, 131–145. doi: 10.5194/tc-2-13 1-2008

Aniya, M. (1988). Glacier inventory for the northern Patagonia Icefield, Chile, and variations 1944/45 to 1985/86. *Arctic Alp. Res.* 20, 179–187. doi: 10.2307/1551496

Aniya, M. (1995). Holocene glacial chronology in Patagonia: tyndall and upsala glaciers. *Arctic Alp. Res.* 27, 311–322. doi: 10.2307/1552024

Aniya, M. (1996). Holocene variations of Ameghino Glacier, southern Patagonia. *Holocene* 6, 247–252. doi: 10.1177/095968369600600211

Aniya, M. (2013). Holocene glaciations of Hielo Patagónico (Patagonia Icefield), South America: a brief review. *Geochem. J.* 47, 97–105. doi: 10.2343/geochemj.1.0171

Aniya, M., Naruse, R., Shizukuishi, M., Skvarca, P., and Casassa, G. (1992). Monitoring recent glacier variations in the Southern Patagonia Icefield, utilizing remote sensing data. *Int. Arch. Photogramm. Remote Sens.* 29, 87–94.

Aniya, M., and Skvarca, P. (2012). Little ice age advances of glaciar perito moreno, hielo patagónico sur, South America. *Bull. Glaciol. Res.* 30, 1–8. doi: 10.5331/bgr.30.1

Araneda, A., Torrejón, F., Aguayo, M., Torres, L., Crues, F., Cisternas, M., et al. (2007). Historical records of San Rafael glacier advances (North Patagonian Icefield): another clue to 'Little Ice Age' timing in southern Chile? *Holocene* 17, 987–998. doi: 10.1177/0959683607082414

Aravena, J. C. (2007). Reconstruction of climate variability from tree-ring records and glacier fluctuations in the southern Chilean Andes. Ph.D. thesis, University of Western Ontario, London, ON.

Barcaza, G., Nussbaumer, S. U., Tapia, G., Valdès, J., Gacìa, J. L., Videla, Y., et al. (2017). Glacier inventory and recent glacier variations in the Andes of Chile, South America. *Ann. Glaciol.* 58, 1–15. doi: 10.1017/aog.2017.28

Bolch, T., Menounos, B., and Wheate, R. (2010a). Landsat-based inventory of glaciers in western Canada, 1985–2005. *Remote Sens. Environ.* 114, 127–137. doi: 10.1016/j.rse.2009.08.015

Bolch, T., Yao, T., Kang, S., Buchroithner, M. F., Scherer, D., Maussion, F., et al. (2010b). A glacier inventory for the western nyainqentanglha range and the nam co basin, tibet, and glacier changes 1976–2009. *Cryosphere* 4, 419–433. doi: 10.5194/tc-4-419-2010

Bown, F., Rivera, A., Zenteno, P., Bravo, C., and Cawkwell, F. (2015). "First glacier inventory and recent glacier variations on Isla Grande de Tierra del Fuego and adjacent islands in Southern Chile," in *Global Land Ice Measurements From Space,* eds J. S. Kargel, G. J. Leonard, M. P. Bishop, A. Kääb, and B. H. Raup (Heidelberg; Berlin: Springer), 661–673.

Bräuning, A. (2006). Tree-ring evidence of Little Ice Age glacier advances in southern Tibet. *Holocene* 16, 369–380. doi: 10.1191/0959683606hl922rp

Carrasco, J., Casassa, G., and Rivera, A. (2000). "Meteorological *in situ* observation in the southern ice cap, Patagonia," in *Proceedings of the 6th International Conference on Southern Hemisphere Meteorology and Oceanography*. Santiago: American Meteorological Society, 300–301.

Carrasco, J., Casassa, G., and Rivera, A. (2002). "Meteorological and climatological aspect of the Southern Patagonia Icefield," in *The Patagonia Icefields*, eds G. Casassa, F. V. Sepúlveda, and R. M. Sinclair (New York, NY: Kluwer-Plenum). 29–41.

Casassa, G., Rodriguez, J. L., and Loriaux, T. (2014). "A new glacier inventory for the Southern Patagonia icefield and areal changes 1986-2000," in *Global Land Ice Measurements From Space,* eds J. S. Kargel, G. J. Leonard, M. P. Bishop, A. Kääb, and B. H. Raup (Heidelberg; Berlin: Springer), 639–660.

Davies, B. J., and Glasser, N. F. (2012). Accelerating shrinkage of Patagonian glaciers from the "Little Ice Age" (c. AD 1870) to 2011). *J. Glaciol.* 58, 1063–1084. doi: 10.3189/2012JoG12J026

De Angelis, H. (2014). Hypsometry and sensitivity of the mass balance to changes in equilibrium-line altitude: the case of the Southern Patagonia Icefield. *J. Glaciol.* 60, 14–28. doi: 10.3189/2014JoG13J127

Dollenz, O. (1991). Sucesion vegetal en el sistema morrenico del Glaciar Dickson, Magallanes, Chile. *Anales Insituto de la Patagonia Seria Ciencias Naturales* 20, 50–60.

Dussaillant, I., Berthier, E., and Brun, F. (2018). Geodetic mass balance of the Northern Patagonian Icefield from 2000 to 2012 using two independent methods. *Front. Earth Sci.* 6:8. doi: 10.3389/feart.2018.00008

Falaschi, D., Bravo, C., Masiokas, M., Villalba, R., and Rivera, A. (2013). First Glacier inventory and recent changes in glacier area in the monte san lorenzo region (47°S), Southern Patagonian Andes, South America. *Arct. Antarct. Alp. Res.* 45, 19–28. doi: 10.1657/1938-4246-45.1.19

Fischer, M., HussChloé Barboux, M., and Hoelzle, M. (2014). The new swiss glacier inventory SGI2010: relevance of using high-resolution source data in areas dominated by very small glaciers. *Arct. Antarct. Alp. Res.* 46, 933–945. doi: 10.1657/1938-4246-46.4.933

Garreaud, R., Lopez, P.;, Minvielle, M., and Rojas, M. (2013). Large-scale control on the patagonian climate. *J. Clim.* 26, 215–230. doi: 10.1175/JCLI-D-12-00001.1

Glasser, N. F., Harrison, S., Jansson, K. N., Anderson, K., and Cowley, A. (2011). Global sea-level contribution from the Patagonian Icefields since the Little Ice Age maximum. *Nat. Geosci.* 4, 303–307. doi: 10.1038/ngeo1122

Granshaw, F. D., and Fountain, A. G. (2006). Glacier change (1958–1998) in the North Cascades National Park Complex, Washington, USA. *J. Glaciol.* 52, 251–256. doi: 10.3189/172756506781828782

Guo, W., Liu, S., Xu, J., Wu,. L., Shangguan, D., Yao, X., et al. (2015). The second Chinese glacier inventory: data, methods and results. *J. Glaciol.* 61, 357–372. doi: 10.3189/2015JoG14J209

Harrison, S., Glasser, N. F., Duller, G. A. T., and Jansson, K. N. (2012). Early and mid-holocene age for the tempanos moraines, Laguna San Rafael, Patagonian Chile. *Quat. Sci. Rev.* 31, 82–92. doi: 10.1016/j.quascirev.2011.10.015

Harrison, S., Glasser, N. F., Winchester, V., Haresign, E., Warren, C., Duller, G. A. T., et al. (2008). Glaciar León, Chilean Patagonia: late-Holocene chronology and geomorphology. *Holocene* 18, 643–652. doi: 10.1177/0959683607 086771

Harrison, S., and Winchester, V. (1998). Historical fluctuations of the Gualas and Reicher Glaciers, North Patagonian Icefield, Chile. *Holocene* 8, 481–485. doi: 10.1191/095968398672334459

Harrison, S., and Winchester, V. (2000). Nineteenth- and twentieth century glacier fluctuations and climatic implications in the Arco and Colonia Valleys, Hielo Patagónico Norte, Chile. *Arct. Antarct. Alp. Res.* 32, 55–63. doi: 10.2307/1552410

Harrison, S., Winchester, V., and Glasser, N. F. (2007). The timing and nature of recession of outlet glaciers of Hielo Patagónico Norte, Chile, from their Neoglacial IV (Little Ice Age) maximum positions. *Glob. Planet. Change* 59, 67–78. doi: 10.1016/j.gloplacha.2006.11.020

Heusser, C. J. (1964). "Some pollen profiles from Laguna de San Rafael area, Chilem," in *Ancient Pacific Flora; the Pollen Story,* ed L. M. Cranwell (Honolulu: University of Hawaii Press), 95–115.

Hochreuther, P., Loibl, D., Wernicke, J., Zhu, H., Grießinger, J., and Bräuning, A. (2015). Ages of major Little Ice Age glacier fluctuations on the southeast Tibetan plateau derived from tree-ring-based moraine dating. *Palaeogeogr. Palaeoclimatol. Palaeoecol.* 422, 1–10. doi: 10.1016/j.palaeo.2015.01.002

Holmlund, P., and Fuenzalida, H. (1995). Anomalous glacier responses to 20th century climatic changes in Darwin Cordillera, southern Chile. *J. Glaciol.* 41, 465–473. doi: 10.1017/S0022143000034808

Koch, J. (2015). Little Ice Age and recent glacier advances in the Cordillera Darwin, Tierra del Fuego, Chile. *Anal. Instituto Patagonia* 43, 127–136. doi: 10.4067/S0718-686X2015000100011

Koch, J., and Kilian, R. (2005). Little Ice Age glacier fluctuations, Gran Campo Nevado, southernmost Chile. *Holocene* 15, 20–28. doi: 10.1191/0959683605hl780rp

Koppes, M., Hallet, B., and Anderson, J. (2009). Synchronous acceleration of ice loss and glacial erosion, Glaciar Marinelli, Chilean Tierra del Fuego. *J. Glaciol.* 55, 207–220. doi: 10.3189/002214309788608796

Kuylenstierna, J., Rosqvist, G. C., and Holmlund, P. (1996). Late- Holocene glacier variations in the Cordillera Darwin, Tierra del Fuego, Chile. *Holocene* 6, 353–358. doi: 10.1177/095968369600600310

Lenaerts, J. T. M., Van den Broeke, M. R., Van Wessem, J. M., and Van de Berg, W. J. (2014). Extreme precipitation and climate gradients in Patagonia revealed by high-resolution regional atmospheric climate modeling. *J. Clim.* 27, 4607–4621. doi: 10.1175/JCLI-D-13-00579.1

Lopez, P., Chevallier, P., Favier, V., Pouyaud, B., Ordenes, F., and Oerlemans, J. (2010). A regional view of fluctuations in glacier length in southern South America. *Glob. Planet. Change* 71, 85–108. doi: 10.1016/j.gloplacha.2009.12.009

Malz, P., Meier, W., Casassa, G., Jaña, R., Skvarca, P., and Braun, M. H. (2018). Elevation and mass changes of the Southern Patagonia Icefield Derived from TanDEM-X and SRTM Data. *Remote Sens.* 10:188. doi: 10.3390/rs10020188

Masiokas, M. H., Delgado, S., Pitte, P., Berthier, E., Villalba, R., Skvarca, P., et al. (2015). Inventory and recent changes of small glaciers on the northeast margin of the Southern Patagonia Icefield, Argentina. *J. Glaciol.* 61, 511–523. doi: 10.3189/2015JoG14J094

Masiokas, M. H., Luckman, B. H., Villalba, R., Delgado, S., Skvarca, P., and Ripalta, A. (2009a). Little Ice Age fluctuations of small glaciers in the Monte Fitz Roy and Lago del Desierto areas, south Patagonian Andes, Argentina. *Palaeogeogr. Palaeoclimatol. Palaeoecol.* 281, 1351–1362. doi: 10.1016/j.palaeo.2007.10.031

Masiokas, M. H., Rivera, A., Espizua, L. E., Villalba, R., Delgado, S., and Aravena, J. C. (2009b). Glacier fluctuations in extratropical South America during the past 1000 years. *Palaeogeogr. Palaeoclimatol. Palaeoecol.* 281, 242–268. doi: 10.1016/j.palaeo.2009.08.006

Mercer, J. H. (1970). Variations of some Patagonian glaciers since the Late-Glacial; II. *Am. J. Sci.* 269, 1–25. doi: 10.2475/ajs.269.1.1

Messager, M. L., Lehner, B., Grill, G., Nedeva, I., and Schmitt, O. (2016). Estimating the volume and age of water stored in global lakes using a geo-statistical approach. *Nat. Commun.* 7:13603. doi: 10.1038/ncomms13603

Mouginot, J., and Rignot, E. (2015). Ice motion of the Patagonian Icefields of South America. *Geophys. Res. Lett.* 42, 1441–1449. doi: 10.1002/2014GL062661

Moy, C. M., Moreno, P. I., Dunbar, R. B., and Haberzettl, T. (2009). "Past climate variability in South America and surrounding regions: from the Last Glacial Maximum to the Holocene," in *Past Climate Variability in South America and Surrounding Regions: From the Last Glacial Maximum to the Holocen*, eds F. Vimeux, F. Sylvestre, and M. Khodri (New York, NY: Springer), 353–392.

Paul, F., and Andreassen, L. M. (2009). A new glacier inventory for the Svartisen region, Norway, from Landsat ETM+ data: challenges and change assessment. *J. Glaciol.* 55, 607–618. doi: 10.3189/002214309789471003

Paul, F., Barrand, N. E., Berthier, E., Bolch, T., Casey, K., Frey, H., et al. (2013). On the accuracy of glacier outlines derived from remote-sensing data. *Ann. Glaciol.* 54, 171–182. doi: 10.3189/2013AoG63A296

Paul, F., Barry, R. G., Cogley, J. G., Frey, H., Haeberli, W., Ohmura, A., et al. (2009). Recommendations for the compilation of glacier inventory data from digital sources. *Ann. Glaciol.* 50, 119–126. doi: 10.3189/172756410790595778

Paul, F., Bolch, T., Briggs, K., Kääb, A., McMillan, M., McNabb, R., et al. (2017). Error sources and guidelines for quality assessment of glacier area, elevation change, and velocity products derived from satellite data in the Glaciers_cci project. *Remote Sens. Environ.* 2003, 256–275. doi: 10.1016/j.rse.2017.08.038

Paul, F., Bolch, T., Kääb, A., Nagler, T., Nuth, C., Scharrer, K., et al. (2015). The glaciers climate change initiative: methods for creating glacier area, elevation change and velocity products. *Remote Sens. Environ.* 162, 408–426. doi: 10.1016/j.rse.2013.07.043

Paul, F., and Hendriks, J. (2010). "Optical remote sensing of glaciers," in *Remote Sensing of Glaciers - Techniques for Topographic, Spatial and Thematic Mapping of Glaciers,* eds P. Pellikka, and W. G. Rees (Leiden: CRC Press, Taylor and Francis Group), 137–152.

Paul, F., Huggel, C., Kääb, A., Kellenberger, T., and Maisch, M. (2003). "Comparison of TM-derived glacier areas with higher resolution data sets. EARSeL eProceedings 2, 15-21," in *Proceedings of the EARSeL Workshop on Remote Sensing of Land Ice and Snow* (Berne).

Paul, F., and Mölg, N. (2014). Hasty retreat of glaciers in northern Patagonia from 1985 to 2011. *J. Glaciol.* 60, 1033–1043. doi: 10.3189/2014JoG14J104

Pfeffer, T. W., Arendt, A. A., Bliss, A., Bolch, T., Cogley, J. G., Gardner, A. S., et al. (2014). The randolph glacier inventory: a globally complete inventory of glaciers. *J. Glaciol.* 60, 537–552. doi: 10.3189/2014JoG13J176

Pisano, E. (1978). Establecimiento de Nothofagus betuloides (Mirb.) Blume (Coigue de Magallanes) en un valle en proceso de desglaciacion. *Anales del Insituto de la Patagonia* 9, 107–128.

Rabatel, A. J. L., Ceballos, N., Micheletti, E., Jordan, M., and Braitmeier, J., Gonzalez, N. et al. (2018). Toward an imminent extinction of Colombian glaciers? *Geogr. Ann. A Phys. Geogr.* 100, 75–95. doi: 10.1080/04353676.2017.1383015

Raup, B., and Khalsa, S. J. S. (2007). *GLIMS Analysis Tutorial, vers. 22/05/2007 (pp. 15).* Boulder: NSIDC. Available online at: http://glims.org/MapsAndDocs/assets/GLIMS_Analysis_Tutorial_a4.pdf

Randolph Glacier Inventory Consortium (2017). *Randolph Glacier Inventory – A Dataset of Global Glacier Outlines: Version 6.0: Technical Report, Global Land Ice Measurements from Space*, Digital Media.

Rignot, E., Rivera, A., and Casassa, G. (2003). Contribution of the patagonia icefields of south america to sea level rise. *Science* 302, 434–437. doi: 10.1126/science.1087393

Rivera, A., Aravena, J. C., and Casassa, G. (1997). Recent fluctuations of glaciar Pío XI, patagonia: discussion of a glacial surge hypothesis. *Mount. Res. Dev.* 17, 309–322. doi: 10.2307/3674021

Rivera, A., Benham, T., Casassa, G., Bamber, J., and Dowdeswell, J. (2007). Ice elevation and areal changes of glaciers from the Northern Patagonia Icefield, Chile. *Glob. Planet. Change* 59, 126–137. doi: 10.1016/j.gloplacha.2006.11.037

Rivera, A., and Casassa, G. (2004). Ice elevation, areal and frontal changes of glaciers from National Park Torres del Paine, Southern Patagonia Icefield. *Arct. Antarct. Alp. Res.* 36, 379–389. doi: 10.1657/1523-0430(2004)036[0379:IEAAFC]2.0.CO;2

Rivera, A., Koppes, M., Bravo, C., and Aravena, J. C. (2012). Little Ice Age advance and retreat of Glaciar Jorge Montt, Chilean Patagonia, recorded in maps, air photographs and dendrochronology. *Climate Past* 8, 403–414. doi: 10.5194/cp-8-403-2012

Sakakibara, D., and, Sugiyama S. (2014). Ice-front variations and speed changes of calving glaciers in the Southern Patagonia Icefield from 1984 to 2011. *J. Geophys. Res. Earth Surf.* 119, 2541–2554. doi: 10.1002/2014JF003148

Scasso, R. A., Corbella, H., and Tiberi, P. (1994). Sedimentological analysis of the tephra from the 12-15 August 1991 eruption of Hudson volcano. *Bull. Volcanol.* 56, 121–132. doi: 10.1007/BF00304107

Schneider, C., Glaser, M., Kilian, R., Santana, A., Butorovic, N., and Casassa, G. (2003). Weather observations across the southern Andes at 53°S. *Phys. Geogr.* 24, 97–119. doi: 10.2747/0272-3646.24.2.97

Schneider, C., Schnirch, M., Acu-a, C., and Kilian, R. (2007). Glacier inventory of the Gran Campo Nevado Ice Cap in the Southern Andes and glacier changes observed during recent decades. *Glob. Planet. Change* 59, 87–100. doi: 10.1016/j.gloplacha.2006.11.023

Smith, B., and Sandwell, D. (2003). Accuracy and resolution of shuttle radar topography mission data. *Geophys. Res. Lett.* 30, 1–4. doi: 10.1029/2002GL016643

Smith, R. B., and Evans, J. P. (2007). Orographic precipitation and water vapor fractionation over the southern Andes. *J. Hydrometeorol.* 8, 3–19. doi: 10.1175/JHM555.1

Strelin, J., Casassa, G., Rosqvist, G., and Holmlund, P. (2008). Holocene glaciations in the Ema Glacier valley, Monte Sarmiento Massif, Tierra del Fuego. *Palaeogeogr. Palaeoclimatol. Palaeoecol.* 260, 299–314. doi: 10.1016/j.palaeo.2007.12.002

Strelin, J., and Iturraspe, R. (2007). Recent evolution and mass balance of Cordón Martial glaciers, Cordillera Fueguina Oriental. *Glob. Planet. Change* 59, 17–26. doi: 10.1016/j.gloplacha.2006.11.019

Tilling, R. L. (2009). Volcanism and associated hazards: the Andean perspective. *Adv. Geosci.* 22, 125–137. doi: 10.5194/adgeo-22-125-2009

Villalba, R., Lara, A., Boninsegna, J. A., Masiokas, M., Delgado, S., Aravena, J. C., et al. (2003). Large-Scale Temperature Changes across the Southern Andes: 20th-Century Variations in the Context of the Past 400 Years. *Clim. Change* 59, 177–232. doi: 10.1023/A:1024452701153

Wang, W., YOA, T., and Yang, X. (2011). Variations of glacial lakes and glaciers in the Boshula mountain range, southeast Tibet, from the 1970s to 2009. *Ann. Glaciol.* 52, 9–17. doi: 10.3189/172756411797252347

Warren, C. R., Rivera, A., and Post, A. (1997). Greatest Holocene advance of Glaciar Pío XI, Chilean Patagonia: possible causes. *Ann. Glaciol.* 24, 11–15. doi: 10.1017/S026030550001185X

Winchester, V., and Harrison, S. (1996). Recent oscillations of the San Quintin and San Rafael Glaciers, Patagonian Chile. *Geogr. Ann.* 78, 35–49. doi: 10.1080/04353676.1996.11880450

Winchester, V., and Harrison, S. (2000). Dendrochronology and lichenometry: colonization, growth rates and dating of geomorphological events on the east side of the North Patagonian Icefield, Chile. *Geomorphology* 34, 181–194. doi: 10.1016/S0169-555X(00)00006-4

Winchester, V., Harrison, S., and Warren, C. R. (2001). Recent retreat Glacier Nef, Chilean Patagonia, dated by lichenometry and dendrochronology. *Arct. Antarct. Alp. Res.* 33, 266–273. doi: 10.2307/1552233

Conflict of Interest Statement: The authors declare that the research was conducted in the absence of any commercial or financial relationships that could be construed as a potential conflict of interest.